A&A, 705, A147 (2026)
https://doi.org/10.1051/0004-6361/202555596

Astronomy & Astrophysics

A weak Lyα halo for an extremely bright little red dot

Indications of enshrouded supermassive black hole growth

Alberto Torralba[1,⋆], Jorryt Matthee[1], Gabriele Pezzulli[2], Tanya Urrutia[3], Max Gronke[4], Sara Mascia[1], Francesco D'Eugenio[5,6], Claudia Di Cesare[1], Anna-Christina Eilers[7], Jenny E. Greene[8], Edoardo Iani[1], Yuzo Ishikawa[7], Ruari Mackenzie[9], Rohan P. Naidu[7], Benjamín Navarrete[1], and Gauri Kotiwale[1]

[1] Institute of Science and Technology Austria (ISTA), Am Campus 1, 3400 Klosterneuburg, Austria
[2] Kapteyn Astronomical Institute, University of Groningen, Landleven 12, 9747 AD Groningen, The Netherlands
[3] Leibniz-Institut für Astrophysik, Potsdam, An der Sternwarte 16, Potsdam 14482, Germany
[4] Max Planck Institute for Astrophysics, Karl-Schwarzschild-Str. 1, 85748 Garching, Germany
[5] Kavli Institute for Cosmology, University of Cambridge, Madingley Road, Cambridge CB3 0HA, United Kingdom
[6] Cavendish Laboratory – Astrophysics Group, University of Cambridge, 19 JJ Thomson Avenue, Cambridge CB3 0HE, United Kingdom
[7] MIT Kavli Institute for Astrophysics and Space Research, Massachusetts Institute of Technology, Cambridge, MA 02139, USA
[8] Department of Astrophysical Sciences, Princeton University, Princeton, NJ 08544, USA
[9] Institute of Physics, Laboratory of Astrophysics, Ecole Polytechnique Fédérale de Lausanne (EPFL), Observatoire de Sauverny, 1290 Versoix, Switzerland

Received 20 May 2025 / Accepted 4 November 2025

ABSTRACT

The abundant population of little red dots (LRDs), compact objects with red UV to optical colors and broad Balmer lines at high redshift, is revealing new insights into the properties of early active galactic nuclei (AGN). Perhaps the most surprising features of this population are the presence of Balmer absorption and ubiquitous strong Balmer breaks. Recent models link these features to an active supermassive black hole (SMBH) cocooned in very dense gas ($N_{\rm H} \sim 10^{24}\,{\rm cm}^{-2}$). We present a stringent test of such models using VLT/MUSE observations of A2744-45924, the most luminous LRD known to date ($L_{\rm H\alpha} \approx 10^{44}\,{\rm erg\,s}^{-1}$), located behind the Abell-2744 lensing cluster at $z = 4.464$ ($\mu = 1.8$). We detect a moderately extended Lyα nebula ($h \approx 5.7$ pkpc), spatially offset from the point-like Hα seen by JWST by ≈1.6 pkpc. The Lyα emission is narrow (FWHM = 270 ± 15 km s^{-1}), and faint (Lyα = 0.07Hα) compared to Lyα nebulae typically observed around quasars of similar luminosity. We detect compact N IV]λ1486 emission, spatially aligned with Hα, and a spatial shift in the far-UV continuum matching the Lyα offset. We discuss that Hα and Lyα have distinct physical origins: Hα originates from the AGN, while Lyα is powered by star formation. In the environment of A2744-45924, we identified four extended Lyα halos ($\Delta z < 0.02$, $\Delta r < 100$ pkpc). Their Lyα luminosities match the expectations based on Hα emission, and show no evidence for radiation from A2744-45924 affecting its surroundings. The lack of strong, compact, and broad Lyα and the absence of a luminous extended halo, suggest that the UV AGN light is obscured by dense gas cloaking the SMBH with a covering factor close to unity.

Key words. galaxies: active – galaxies: halos – galaxies: high-redshift

1. Introduction

JWST's significantly increased sensitivity in near-infrared imaging and spectroscopy is offering a new perspective on galaxies in the distant Universe (see Adamo et al. 2025, for an overview). One of the most debated discoveries since the first data arrived in 2022 is the nature of a loosely defined class of objects that became known as the little red dots (LRDs; Matthee et al. 2024). These objects are characterized by their compact morphologies and red rest-frame optical colors, often in combination with blue UV colors resulting in a particular V shape (e.g., Labbe et al. 2025; Akins et al. 2025b; Kokorev et al. 2024a; Barro et al. 2024). To date, ∼1000 LRDs have been photometrically identified over redshifts $z \approx 2$–9 spanning luminosities $L_{\rm H\alpha} \sim 10^{41-44}\,{\rm erg\,s}^{-1}$, with number densities $\sim 10^{-5}$ to $10^{-4}\,{\rm cMpc}^{-3}$ (e.g., Harikane et al. 2023; Akins et al. 2025b; Kokorev et al. 2024a; Greene et al. 2024; Maiolino et al. 2024a; Matthee et al. 2024; Kocevski et al. 2025; Lin et al. 2025), 1000 to 10 000 times higher than those of UV-selected quasars at similar redshifts (e.g., Niida et al. 2020; Matsuoka et al. 2023). These numbers imply that they constitute a significant fraction of the galaxy population (∼1%). These high number densities and their moderate overdensities (e.g., Pizzati et al. 2025; Matthee et al. 2025; Arita et al. 2025) suggest that the majority of LRDs reside in relatively low-mass galaxies in low-mass halos ($M_{\rm star} \sim 10^8\,M_\odot$, $M_{\rm halo} \sim 10^{11}\,M_\odot$). In many cases the Balmer emission lines show significant broad components with widths >1000 km s^{-1} (e.g., Kocevski et al. 2023; Matthee et al. 2024; Taylor et al. 2025a; Lin et al. 2024), which are indicative of AGN activity (e.g., Pérez-González et al. 2024; Kokorev et al. 2024b; Leung et al. 2025; Volonteri et al. 2025). Other AGN indicators are the detection of high-ionization UV lines (Treiber et al. 2025) and Fe II

⋆ Corresponding author: alberto.torralba@ista.ac.at

emission (Labbe et al. 2024) and indications of time variability in the Balmer emission lines (Ji et al. 2025; Furtak et al. 2025) and in the Balmer Break strength (Ji et al. 2025) in select LRDs. On the other hand, LRDs typically lack the IR emission associated with a hot torus (e.g., Williams et al. 2024; Akins et al. 2025b; Setton et al. 2025), and they also show weak or no radio (e.g., Latif et al. 2025; Perger et al. 2025; Gloudemans et al. 2025; Mazzolari et al. 2026) and X-ray emission (e.g., Yue et al. 2024; Ananna et al. 2024; Maiolino et al. 2025).

A particularly intriguing feature observed in a significant subset of LRDs is the presence of strong narrow Balmer absorption in the Hα and Hβ lines (e.g., Matthee et al. 2024; Juodžbalis et al. 2024; Taylor et al. 2025a; D'Eugenio et al. 2025), along with a pronounced Balmer break appearing consistently at rest-frame wavelengths ≈3645 Å (e.g., Setton et al. 2024; Wang et al. 2024). These two properties may be correlated and can be explained by very dense gas along the line of sight ($n_{\rm H} \sim 10^9\,{\rm cm}^{-3}$ and column densities $N_{\rm H} \sim 10^{24}\,{\rm cm}^{-2}$; e.g., Inayoshi & Maiolino 2025; Ji et al. 2025; Naidu et al. 2025; Taylor et al. 2025b), which could also explain the X-ray weakness (e.g., Kocevski et al. 2023) as being due to Compton thick absorption (e.g., Juodžbalis et al. 2024; Maiolino et al. 2025). The abrupt and consistent Balmer break of many LRDs could otherwise only be explained by classical models with a very unusual and specific combination of young and old stellar populations and dust attenuation laws (e.g., Wang et al. 2024; Labbe et al. 2024, 2025; Ma et al. 2025). Moreover, the strongest Balmer breaks observed cannot be reproduced by stellar population models, even assuming extreme dust attenuation laws (de Graaff et al. 2025; Naidu et al. 2025).

Recent studies have proposed models in which a very dense, turbulent, and dust-free gas completely cocoons the supermassive black hole (SMBH) of LRDs (*Black Hole Star* models; BH*; Naidu et al. 2025; Rusakov et al. 2025; de Graaff et al. 2025). In these models, the observed Balmer line profiles could have been broadened partly by scattering in the dense gas (Rusakov et al. 2025; Naidu et al. 2025). This would imply that the single epoch virial estimators of black hole (BH) mass cannot be simply applied to the broad components of the emission lines, implying that the BH mass is overestimated; this has significant implications for the interpretation of the BH-stellar mass relation (cf. Pacucci & Loeb 2024). However, it remains an open question whether the dense gas fully obscures the central SMBH (covering factor $f_{\rm cov} \sim 1$) or whether the absorption arises from an irregular distribution of clouds along the line of sight ($f_{\rm cov} < 1$). Assessing the covering factor is crucial to understanding SMBH growth at high redshift, offering insights into the rapid early assembly of black holes in the very early Universe. Determining $f_{\rm cov}$ is also essential for evaluating the impact of AGN on their surroundings, particularly whether they produce enough ionizing photons to significantly contribute to cosmic reionization.

A detailed study of the UV spectrum of LRDs is key to determining $f_{\rm cov}$. In particular, the strength, spatial distribution, and spectral profile of the Lyman-alpha (Lyα) emission line are highly sensitive to the presence and distribution of neutral gas (e.g., Neufeld 1990; Steidel et al. 2011). If $f_{\rm cov} \ll 1$, the escape fraction of Lyα and ionizing photons must be high; therefore, we would expect to see large and luminous Lyα nebulae around LRDs, similar to the ones seen around luminous quasars. On the contrary, if $f_{\rm cov}$ is close to unity, the extremely dense gas would strongly suppress Lyα emission and the ionizing continuum, and the Lyα halo would be weak.

In this work we present deep VLT/MUSE observations of A2744-45924, the most luminous LRD known (Greene et al. 2024; Labbe et al. 2024); these observations provide the first Lyα halo study of an LRD and its environment. MUSE has demonstrated the existence of large Lyα halos around quasars (e.g., Borisova et al. 2016), which are powered by elevated photoionization levels in the vicinity of quasars. The surface brightness depends slightly on UV luminosity (e.g., Mackenzie et al. 2021) and Type II AGN tend to have more elongated halos (e.g., den Brok et al. 2020), exemplifying the use of extended Lyα nebulae to probe AGN covering factors and escaping ionizing luminosity. The Lyα surface brightness around quasars is significantly elevated compared to Lyα halos around star-forming galaxies (e.g., Leclercq et al. 2017). The key questions that we aim to answer include the influence of the AGN on the circumgalactic medium (CGM) gas, and what the covering factor of A2744-45924's central SMBH is.

This paper is structured as follows. In Sect. 2 we describe the observational data from VLT/MUSE and JWST/NIRCam used throughout this work. In Sect. 3 we describe the spatially resolved properties of the rest-frame UV spectrum of A2744-45924. In Sect. 4 we analyze the Lyα emission of the galaxies in the environment of A2744-45924. In Sect. 5 we discuss the implications of our results for the interpretation of the origin of the Lyα emission. In Sect. 6 we discuss the possible interpretations of our results in the context of LRD models involving dense gas enshrouded SMBH growth. Finally, in Sect. 7 we summarize our main findings.

Throughout this work we use a ΛCDM cosmology as described by Planck Collaboration VI (2020), with $\Omega_\Lambda = 0.69$, $\Omega_{\rm M} = 0.31$, and $H_0 = 67.7\,{\rm km\,s^{-1}\,Mpc^{-1}}$. All photometric magnitudes are given in the AB system (Oke & Gunn 1983).

2. Data

2.1. JWST

Among the LRD population, A2744-45924 stands out for its luminosity $L_{\rm H\alpha} \approx 10^{44}\,{\rm erg\,s^{-1}}$ (Labbe et al. 2024), which places it in the (obscured) quasar regime. Found behind the lensing cluster Abell-2744 (A2744 Abell et al. 1989) at $z \approx 4.464$, A2744-45924 is magnified by a factor $\mu = 1.8$, with $\mu_t = 1.684$ and $\mu_r = 1.072$ being the transverse and radial magnification, respectively, relative to $\theta = 19.9°$ (Furtak et al. 2023; Price et al. 2025).

A2744-45924 was first identified in the Cycle 1 Treasury program #2561 (UNCOVER; Bezanson et al. 2024) DR1 images and selected as an LRD based on the compact morphology in the long wavelength and V-shaped SED. NIRSpec/PRISM spectroscopy confirmed the AGN nature through the detection of broad Hα emission (Greene et al. 2024). A2744-45924 was also observed in the JWST Cycle 2 survey #3516 (ALT; Naidu et al. 2024, object ID 66543). The ALT survey targeted the A2744 lensing cluster, taking imaging data over ∼30 arcmin^2 using the NIRCam short-wavelength channel broadband filters F070W and F090W and deep grism observations in F356W. These grism observations covered the Hα line with a resolution of $R \sim 1600$, revealing broad non-Gaussian wings and narrow Hα absorption (Fig. 5 in Labbe et al. 2024).

The NIRCam imaging revealed a compact yet resolved rest-frame UV morphology, along with a more extended and fainter component showing up in the far-UV (Labbe et al. 2024). It shows broad Balmer lines, Hα absorption, a Balmer break and various Fe II emission lines: all signs of AGN activity. Despite

its rest-frame optical luminosity and unlike quasars, A2744-45924 is not strongly detected in the sub-millimeter (neither continuum nor [C II] emission) and the faintness in JWST/MIRI data indicates the lack of hot dust emission (Setton et al. 2025). Akins et al. (2025a) identified faint [C I] emission from neutral gas with ALMA, possibly spatially offset in a similar direction as the extended component in the far UV. Moreover, Chen et al. (2025) studied the extended component of A2744-45924, identifying it as a star-forming galaxy with stellar mass $\log_{10}(M/M_\odot) = 8.17 \pm 0.08$ and blue rest-frame UV colors ($\beta_{\rm UV} = -2.12$). A2744-45924 is located in the largest galaxy overdensity in the A2744 field, as evidenced by the elevated number of Hα emitters in its vicinity ($1 + \delta = 31 \pm 5$, within a radius of 1 cMpc; Matthee et al. 2025).

2.2. MUSE

Here we present new VLT/MUSE observations of A2744-45924. These data were obtained using the VLT/MUSE integral field spectrograph (Bacon et al. 2010) as part of the ESO P114 program 114.27M6 (PI: Matthee). Observations were taken under clear conditions over the 10–31 October 2024 period. We used MUSE with the wide field mode which has a field of view of $1' \times 1'$, nominal wavelength coverage (470–935 nm) and assisted with ground-layer adaptive optics. Individual exposure times were 675s and we rotated the position angle by 90 degrees between every exposure. To improve the background subtraction, we used random dithering offsets between 0.2″ and 1.5″ between each exposure. The pointing was roughly centered on A2744-45924 and the starting PA was 30 degrees to maximize the number of sources with known spectroscopic redshifts from ALT (Naidu et al. 2024) in the pointing. The total exposure time was 18.9 ks.

Basic data reduction was carried out using version 2.8 of the MUSE pipeline (Weilbacher et al. 2020). Each exposure was aligned to the JWST/F070W WCS and resampled onto a common grid. A superflat correction was applied to mitigate slicer stack transition artifacts (see Bacon et al. 2023), and pixels with fewer than 2000 valid wavelength layers were masked. Additional PCA-based sky subtraction was performed using ZAP (Soto et al. 2016). The aligned exposures were then mean-combined voxel by voxel using a 6σ clipping threshold. In the final cube, we applied a DC offset correction to bring empty sky regions to zero, and replaced the formal variance with an empirically estimated effective variance that accounts for nonpropagated covariances (Urrutia et al. 2019; Weilbacher et al. 2020).

The astrometric corrections and the effective PSF of the MUSE datacube were derived using the JWST F070W image as a reference. This broadband filter includes the wavelength of Lyα at $z = 4.464$. First, we used the IMPHOT package[1] to reproject the F070W image onto the same RA-Dec grid as the MUSE datacube. Next, we generated a pseudo-broadband image by convolving the MUSE datacube with the JWST F070W filter's transmission cube and aligned it to the JWST counterpart using IMPHOT. This process yielded small astrometric corrections of Δ(RA, Dec) = (−0.01656″, −0.00346″) and an effective PSF FWHM of 0.7396″, assuming a Moffat profile with index $\beta = 2.5$. For this, we assumed that the effective PSF FWHM of the F070W image is significantly smaller than that of MUSE. The spectral resolution at the Lyα wavelength of A2744-45924 is $R \approx 2700$ (Bacon et al. 2017).

[1] https://github.com/musevlt/imphot

Table 1. Collection of relevant properties of the rest-frame UV and Lyα emission of A2744-45924.

Property	Value	Notes
RA	00h 14m 20.34s	a
Dec	−30:20:37.06	a
z	4.464	b
Lyα	20 ± 5	c
N IV]λ1483	0.8 ± 0.5	c
N IV]λ1486	2.5 ± 0.6	c
O III]λ1661	0.9 ± 0.5	c
O III]λ1666	1.9 ± 0.9	$c*$
Hα	310 ± 16	$c\dagger$
N IV]λ1483/N IV]λ1486	0.32 ± 0.21	d
EW$_0$(Lyα)	97 ± 28 Å	e
EW$_0$(N IV]λ1483)	2.8 ± 1.7 Å	e
EW$_0$(N IV]λ1486)	9 ± 2 Å	e
FWHM$_{\rm Ly\alpha}$	270 ± 15 km s^{-1}	f
$\Delta v_{\rm Ly\alpha,red}$	183 ± 5 km s^{-1}	g
$h_{\rm halo}$	5.7 ± 0.7 pkpc	h
$M_{\rm UV,MUSE}$	$-19.39^{+0.12}_{-0.10}$	i

Notes. [a]Right ascension and declination (J2000). [b]Systemic redshift, measured from Hα in NIRCam grism data. [c]Emission line fluxes in units of 10^{-18} erg s^{-1} cm^{-2}, corrected for magnification. [(d)]Flux ratio of the N IV]$\lambda\lambda$1483,1486 doublet. [e]Rest-frame equivalent widths. [f]FWHM of the Lyα emission line. [g]Velocity offset of the Lyα red peak with respect to the Hα systemic redshift. [h]Exponential scale length of the Lyα halo. [i]UV magnitude at 1500 Å, measured from the MUSE 1D spectrum. [*]The flux of O III]λ1666 is affected by a skyline, and may be regarded as an upper limit. [†]From Labbe et al. (2024), added here for completeness.

When analyzing the Lyα emission from galaxies in the large scale environment of A2744-45924, we also make use of deep public MUSE data from Richard et al. (2021) which covers a $2.3 \times 2.3'$ region in the A2744 field centered on the most massive core of the cluster, with no overlap with our main cube. As the JWST coverage is virtually identical, these data serve to increase the statistics.

3. The spatially resolved properties of A2744-45924

Little red dots are compact objects in the rest-frame optical; however, A2744-45924 shows a complex multi-component morphology in the rest-frame UV (Fig. 1). The gentle effective magnification of $\mu = 1.8$ virtually increases the exposure time by a factor $\mu^2 \approx 3$, making A2744-45924 ideal to study its different components to shed light into the relation of SMBHs in LRDs with their host galaxies.

3.1. NIRCam UV morphology

We used the JWST/NIRCam F070W and F090W images to fit the UV morphology of A2744-45924. The purpose of this analysis is to establish a baseline for our MUSE IFU study rather than providing a detailed examination of the UV continuum morphology. At the redshift of A2744-45924 ($z = 4.464$) F070W covers the rest-frame wavelengths 1140–1429 Å (which include Lyα), and F090W covers 1455–1839 Å.

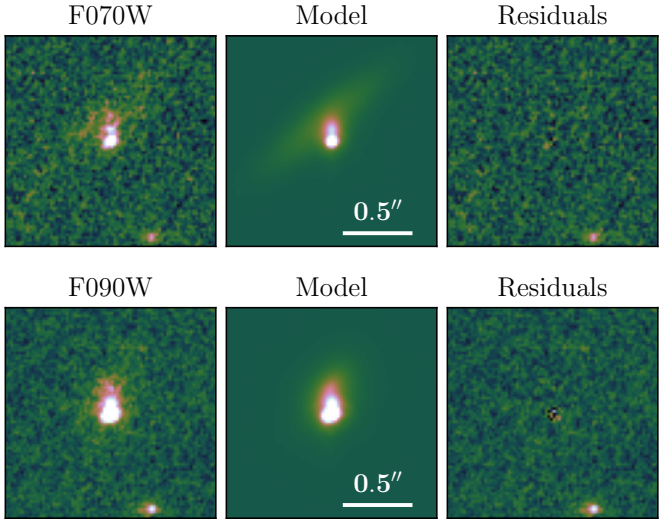

Fig. 1. Morphological model of NIRCam rest-frame UV of A2744-45924 (PSF FWHM ≈0.03″). The left panels display the F070W and F090W stamps, corresponding to central rest-frame wavelengths of approximately 1290 Å and 1651 Å, respectively. The center panels show the best-fit models obtained with IMFIT, while the right panels present the residuals. The F070W image, probing the bluest part of the rest-frame UV spectrum of A2744-45924, including Lyα, reveals a prominent extended component. In contrast, this component is less clear in F090W. An alternative view of the models can be found in Fig. A.1.

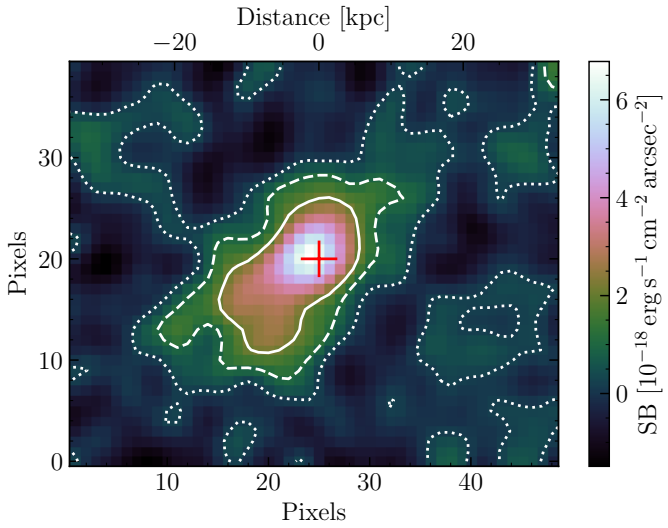

Fig. 2. Surface brightness of the Lyα halo in the wavelength interval 6638.75–6665.00 Å. A 2D Gaussian smoothing kernel is applied across the spatial directions of the cube with σ = 1.5 px. The centroid of the NIRCam Hα emission is marked with a red cross. The dotted, dashed, and solid lines show the surface brightness contours corresponding to a S/N = 1, 5, and 10, respectively. The 1σ SB limit corresponds to 2×10^{-19} erg s^{-1} cm^{-2} arcsec^{-2}.

We used the IMFIT[2] package (Erwin 2015) to fit the morphology of A2744-45924. We tested multi-component models, combinations of 2D elliptical Gaussians and exponentials that minimize χ^2, convolved with the PSF of the corresponding filter – the effective PSFs of the NIRCam images were computed as described in Weibel et al. (2024). The fitted models are shown in Fig. 1. Both F070W and F090W show clear multi-component morphologies. The shape of A2744-45924 in F070W appears to be composed of a compact core plus a more extended and diffuse structure. The core component has two clumps: one well fitted by a Gaussian with σ = 0.016″ (smaller than the PSF, and hence can be considered point-like) and an exponential with scale length 0.05″ (marginally resolved). The extended component is well fitted by a Gaussian with high ellipticity e = 0.73, position angle of θ = 128° and σ = 0.35″. Labbe et al. (2024) similarly fitted a Sérsic profile to this extended component in the F070W image, arguing that its surface brightness (23.5 mag arcsec^{-2}) is much higher than would be expected if it were scattered light from the central source.

Since the F070W filter includes Lyα emission, its morphology may be affected by this emission line. Therefore, we also analyze F090W. The F090W data show a slightly more complex morphology. The core component is best-fitted by three Gaussians (unresolved components with σ = 0.016″, 0.02″, and 0.025″). The F090W image of A2744-45924 also shows a diffuse component, rather extended although less prominent than that of F070W. This extended component is best-fitted with an exponential with a similar position angle of θ = 142°, ellipticity e = 0.36 and scale length h = 0.1″, aligned with the diffuse F070W component, although less extended, hinting that the diffuse component in F070W has bluer UV color – as confirmed by the spatial shift of the continuum emission centroid in the MUSE data (see Sect. 3.2 below). See Appendix A for an alternative fitting procedure in which we attempt to fix the geometrical parameters within both filters.

[2] https://github.com/perwin/imfit

3.2. MUSE spatially resolved UV spectroscopy

Motivated by the complex rest-frame UV morphology seen in the NIRCam images, we examine the spatial distribution of the rest-frame UV continuum emission in the MUSE data. These data cover the rest-frame UV of A2744-45924 up to λ_0 = 1712 Å. We define two spectral intervals: 1235–1430 Å(*cont. blue*) and 1555–1712 Å (*cont. red*), deliberately avoiding the wavelengths of the prominent UV emission lines NIV] and C IV. After integrating the MUSE datacube over these intervals, we observe noticeable offsets between the positions of the two continuum components: Δ(RA, Dec) = (0.15″, 0.22″). We show the collapsed images for the corresponding intervals in Fig. B.1. The offset between *cont. blue* and *cont. red* suggests that the UV continuum of A2744-45924 arises from two distinct components, with the extended one exhibiting bluer colors.

ALMA observations presented in Akins et al. (2025a) revealed narrow (FWHM = 80^{+38}_{-22} km s^{-1}) [C I](2–1) emission from A2744-45924. The [C I] emission appears 0.4″ northeast of the spatial coordinates of the LRD. Akins et al. (2025a) argue that its position is consistent with emission from the phase center given the low S/N of their data. However, we note that this displacement aligns with our spatial centroids of the *cont. blue* and Lyα emission. Thus, the observed shift in [C I] may be physical, suggesting that it originates from the extended associated galaxy and traces its cold gas.

3.3. Extended Lyα emission

We use the MUSE data to characterize extended Lyα emission from A2744-45924. We produce a pseudo-narrowband by collapsing the MUSE datacube along the observed vacuum

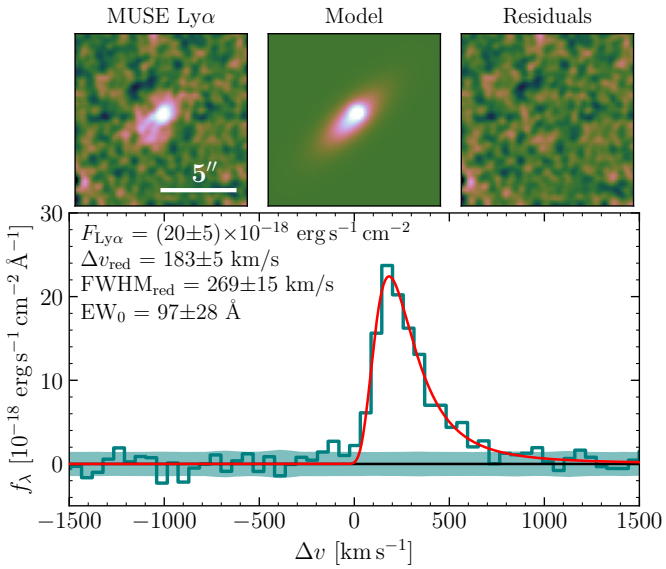

Fig. 3. Lyα spatial morphology and 1D spectrum. *Top*: MUSE pseudo-narrowband of the Lyα emission (left), core+halo model (center), and residuals of the fit (right). The morphology of the Lyα halo is fitted to a two-component model composed of a 2D Gaussian and exponential. The scale length of the exponential component (halo) is h = 5.7±0.7 pkpc, correcting for magnification. *Bottom*: optimally extracted 1D spectrum of Lyα. We show the fitted skewed Gaussian model (red line). The Lyα line shows a narrow single-peaked profile, typical of star-forming galaxies. The bottom axis shows velocities with respect to the systemic redshift of the Hα emission.

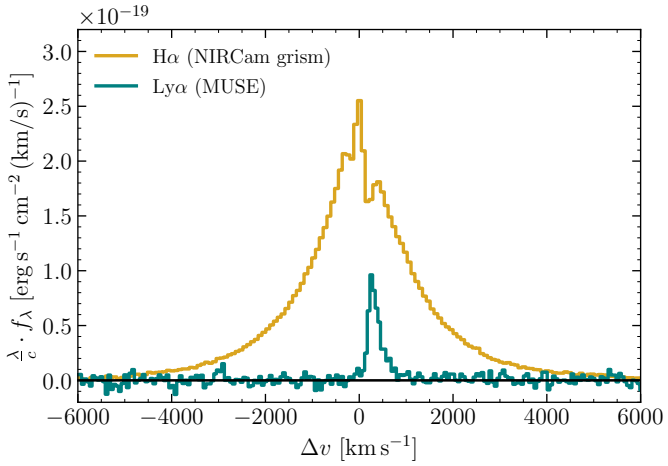

Fig. 4. Flux density in velocity space of the Hα and Lyα lines of A2744-45924, centered on the systemic velocities of the two lines at z = 4.464. The ratio of the line fluxes is Lyα/Hα = 0.066. In addition, Hα has a prominently broad profile (FWHM ≈ 4500 km s^{-1}; Labbe et al. 2024), while Lyα presents the classical shape of a single narrow red peak (FWHM = 270 km s^{-1}; see Fig. 3).

wavelength axis between 6638.75 and 6665.00 Å, covering the red Lyα peak observed in a first optimal extraction (between −165.7 km s and 1019 km s^{-1} with respect to the Hα systemic redshift). We subtract a continuum band, obtained in the same manner in the range 6750–7800 Å (1235–1427 Å in the rest-frame). We choose this wide interval assuming a roughly flat UV continuum ($\beta_{UV} \sim -2$, see Labbe et al. 2024). The result is the continuum subtracted Lyα image shown in the upper left panel of Fig. 2. We fit this image using a two-component model, consisting of a 2D elliptical Gaussian (core) plus a 2D exponential (halo), convolved with the effective PSF of the MUSE datacube (see Sect. 2.2). We also considered adding the fitted F090W morphology as a core component (since this filter does not include Lyα), convolved with the MUSE PSF and appying a scaling factor; however, this component is completely unconstrained in our fits. We therefore conclude that there is no significant Lyα emission from the compact components seen in the NIRCam images (for a similar procedure see Leclercq et al. 2017).

The observed Lyα halo is well fitted by our two-component Gaussian model. We fit an exponential with scale length of 1.28 ± 0.18 arcsec, and ellipticity of e = 0.66 ± 0.06, with an angle of $\theta = (137 \pm 3)°$. For the core Gaussian component we fit FWHM = 0.43″, marginally resolved given the PSF (Sect. 2.2), and implying a size of $r_e \lesssim 2$ pkpc (magnification corrected). The decomposition of both components of the fit is shown in Fig. C.1. To derive the physical geometrical parameters of the exponential halo in the source plane, we apply the radial and transverse magnification corrections (see Sect. 2.1). The halo is more strongly magnified along a direction approximately aligned with the major axis of the observed ellipse. However, even after applying these corrections, the halo remains significantly elliptical, with a scale length of h = 5.7 ± 0.7 pkpc and ellipticity e = 0.56. A schematic representation of the ellipses in the source and image planes is shown in Fig. C.2.

The total flux ratio between the halo and more compact Gaussian component is ∼5.4, indicating that a large fraction of the Lyα flux comes from an extended component. This is opposed to Hα, which presents a point-like morphology centered in the compact UV core (see Labbe et al. 2024). The Lyα halo is consistent with the ones typically found around star-forming galaxies as we discuss in Sect. 5.1.

3.4. Lyα profile

We now turn to the spectral profile of the Lyα emission from A2744-45924. We perform an optimal extraction (Horne 1986) of Lyα using the model fitted as described in Sect. 3.3. The extracted profile is shown in Fig. 3. We fit a skewed Gaussian to the Lyα profile (e.g., Shibuya et al. 2014) obtaining best-fit parameters of v_{red} = 183 ± 5 km s^{-1} (red peak velocity offset), A = (22.7 ± 0.7) × 10^{-18} erg s^{-1} cm^{-2} Å^{-1} (amplitude), $a_{asym.}$ = 0.25 ± 0.02 (asymetry parameter) and FWHM$_{red}$ = 270 ± 15 km s^{-1}. By integrating this best-fit curve, we obtain a total line flux of $F_{Lyα}$ = (20 ± 5) × 10^{-18} erg s^{-1} cm^{-2}, corresponding to a luminosity of 10$^{42.63±0.11}$ erg s^{-1} (magnification corrected flux and luminosity). We compute the EW of the Lyα, first obtaining the continuum flux from the optimally extracted 1D spectrum in the range 1220–1450 Å, after masking sky lines. We measure EW$_{Lyα}$ = 97 ± 28 Å from the MUSE spectrum. We find moderate spatial variations of the fitted skewed Gaussian parameters, with peak velocities ranging from 100 to 200 km s^{-1}, and FWHM from 200 to 300 km s^{-1} across the halo (Fig. D.1). These spectral variations are typical in Lyα halos of star-forming galaxies, and may be related to gas dynamics (e.g., Erb et al. 2018).

In Fig. 4 we compare the absolute fluxes of the Lyα and Hα lines of A2744-45924. We measure a ratio of Lyα/Hα = 0.065 (0.2 if we would consider only the narrow component of Hα fitted in Labbe et al. 2024). This ratio is far from the theoretical Lyα/Hα = 8.7 ratio for f_{esc}(Lyα) = 1, under the traditional assumption of case B recombination and a gas temperature

of $T = 10^4$ K, typical of H II regions. This ratio is also very small in comparison to that measured in composite quasar spectra Lyα/H$\alpha \sim 3$ (Vanden Berk et al. 2001). The Lyα EW and $v_{\mathrm{Ly}\alpha,\mathrm{red}}$ of A2744-45924 are comparable to typical star-forming galaxies in the field (Mascia et al. in prep.).

3.5. Rest-frame UV emission lines

The rest-frame UV spectrum was already covered by the NIRspec/PRISM data presented in Labbe et al. (2024), but the very low spectral resolution ($R \sim 50$–100) of those data challenged the detection and characterization of various emission lines. In the UV spectrum of A2744-45924 in the MUSE data, which has a lower sensitivity but a much higher resolution, we also find a 4σ detection of N IV] λ1486 at a redshift consistent with the Hα redshift. We fit a Gaussian profile to this emission line, and we measure a flux of $F_{\mathrm{N\,IV]}\lambda1486} = (2.5 \pm 0.6) \times 10^{-18}$ erg s^{-1} cm^{-2} (EW$_{\mathrm{N\,IV]}\lambda1486} = 9 \pm 2$ Å). After Lyα, this is the most prominent UV emission line in our data (see Sect. 3.5). By collapsing the MUSE datacube in 10 Åaround the position of N IV] λ1486 we obtain the continuum subtracted stamp shown in the top right panel of Fig. 5. The width of the Gaussian fit to N IV] λ1486 is well resolved as FWHM $= 270 \pm 50$ km s^{-1}. Then, we fit a second Gaussian centered on the expected position of the other component of the N IV] doublet, λ1483, fixing the width of the Gaussian to be the same. We get a tentative flux of $F_{\mathrm{N\,IV]}\lambda1483} = (0.8 \pm 0.5) \times 10^{-18}$ erg s^{-1} cm^{-2} (EW$_{\mathrm{N\,IV]}\lambda1486} = 2.8 \pm 1.7$ Å). We measure a doublet ratio of $f_{1483}/f_{1486} = 0.31 \pm 0.19$, which is suggestive of very high gas density ($n_e > 10^5$ from Fig. 2 in Kewley et al. 2019). Similarly low ratios were also observed in GN-z11 (Maiolino et al. 2024b) and CEERS-1019 (Marques-Chaves et al. 2024), both luminous high-redshift objects with suggested AGN activity.

We also marginally detect the O III]$\lambda\lambda$1661,1666 doublet (individual comopnents with S/N $\approx$ 2). The continuum-subtracted MUSE image suggests a clear detection (bottom right panel of Fig. 5); however, the flux of O III] is affected by a skyline, and may be regarded as an upper limit. The strong N IV] emission, together with the [O III] flux reported in Labbe et al. (2024), suggests a moderate N/O abundance, with $\log_{10}(\mathrm{N/O}) \gtrsim -1.1$ (e.g., Pérez-Montero et al. 2013) under the assumption of an electron temperature $T_e = 10^4$ K. However, deeper observations of both N IV] and O III] are required to robustly determine the N/O ratio, as the O III] fluxes are sensitive to T_e.

Lastly, we neither find significant detection of He II (λ1640) or C IV ($\lambda\lambda$1548,1551). Labbe et al. (2024) measure a C IV flux that is comparable to that of N IV] in the NIRSpec prism spectrum of A2744-45924, yet we do not detect C IV. It is possible that the C IV line is much broader than N IV], hence hindering the detectability in our spectrum. Moreover, several sky lines affect the measurement of this line, as evidenced by the uncertainty spikes in the left panel of the second row of Fig. 5.

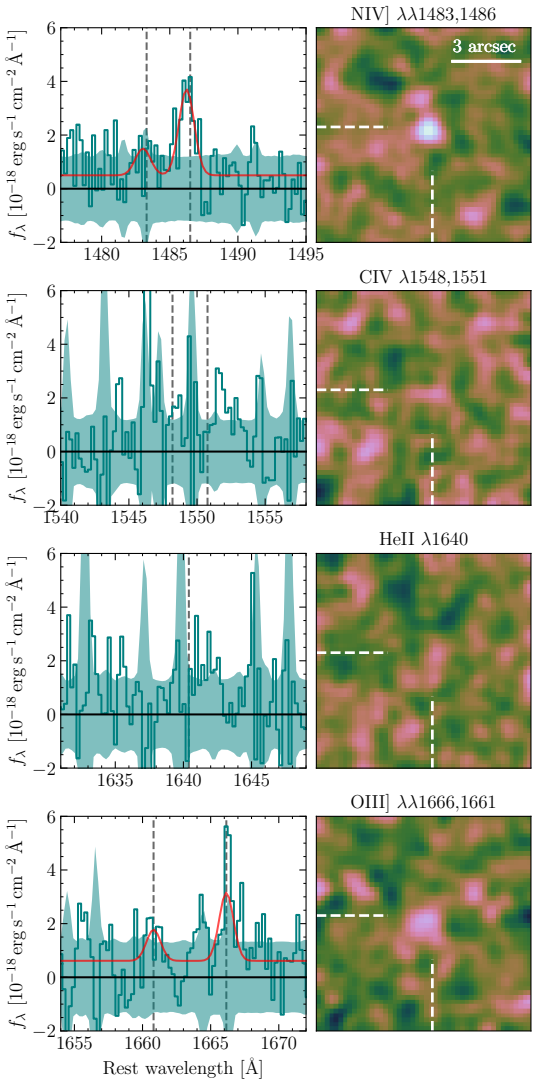

Fig. 5. Rest-frame UV emission lines of A2744-45924. The *left column* shows the 1D spectrum around the wavelength of selected UV emission lines: N IV] ($\lambda\lambda$1483,1486), C IV ($\lambda\lambda$1548,1551), He II (λ1640), and O III] ($\lambda\lambda$1661,1666). In the case of N IV] and O III] the best-fitting two-component Gaussian model with fixed width is also shown. The *right column* shows images obtained collapsing the MUSE datacube in an interval of 10 Åcentered on the selected lines (for doublets, both components stacked), and subtracting the continuum, measured 1000 Åaround the position of the line (masking other emission lines and skylines).

4. Large-scale Lyα emission

We investigate the Lyα emission of other sources in the vicinity of A2744-45924. We identify Lyα halos using the SHINE[3] tool, presented in Tornotti et al. (2025). We look for halos using this tool between observed wavelength 6600 and 6674 Å, corresponding to $z_{\mathrm{Ly}\alpha} = 4.43$–$4.49$ Å. The field of view (FoV) of the MUSE data corresponds to a box with side 1.3′ roughly centered in A2744-45924, hence we probe a volume of ∼172 cMpc^3 (after correcting by the mean magnification of all the sources in the field, $\langle\mu\rangle = 1.8$, with values ranging from 1.5 to 2.9). We use a Gaussian smoothing kernel with $\sigma = 2$ px in the spatial directions, and impose a minimum spatial area of 50 px, 500 minimum connected voxels, and a size between 3 and 100 spectral pixels. After a visual inspection of the output 40 halo candidates produced using SHINE, we identify 4–5 extended Lyα halos between $z \sim 4.45$ and 4.47. These halos are shown in Fig. 6. All the Lyα halos have redshifts consistent with the spectroscopic redshifts of the sources they spatially overlap (Naidu et al. 2024), with expected differences of a few hundred km s^{-1}, in line with the typical shift of Lyα red peaks relative to the systemic redshift. Within the MUSE FoV, we identify five additional sources with spectroscopic redshifts within the

[3] https://github.com/matteofox/SHINE

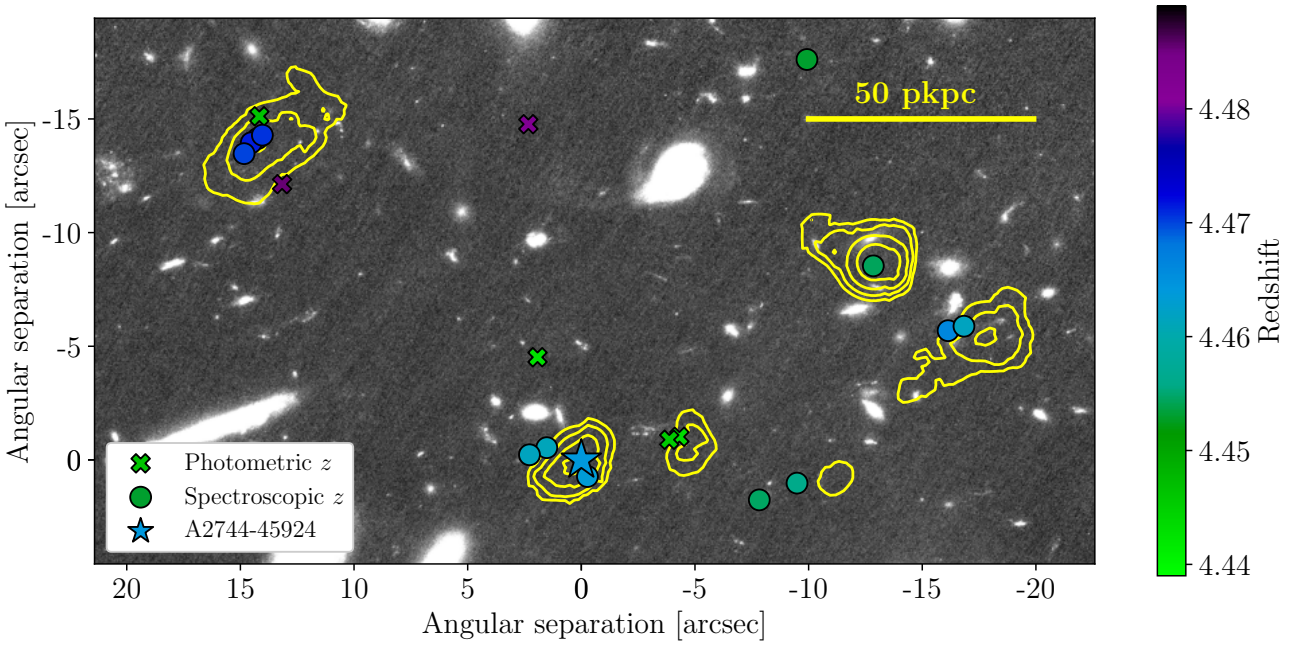

Fig. 6. Detected Lyα halos in the vicinity of A2744-45924. The background image is the NIRCam F070W cutout. The search was performed in a box volume of $\approx$170 cMpc^3 (correcting with the mean magnification of the sources in the field) defined by the FoV of the MUSE data ($1.3' \times 1.3'$); however, we only show a cutout where the halos are detected. We show the contours of the Lyα emission detected at $z = 4.464 \pm 0.02$. Each contour level corresponds to a surface brightness increase by a factor of 1.5 (baseline 1.8×10^{-18} erg s^{-1} cm^{-2} arcsec^{-2}). Also shown are the positions of the JWST objects with spectroscopic (circles) and photometric (crosses) redshift in the same interval (Naidu et al. 2024; Suess et al. 2024). We detect an elevated number of Lyα halos in the environment of A2744-45924; however, this result is consistent with the galaxy overdensity (Matthee et al. 2025). The total flux of Lyα is moderate to low when compared with the total Hα emission of A2744-45924's neighbors (See Fig. 7).

probed interval, but none of them exhibits significant Lyα emission. Additionally, we detect one extra Lyα emitter located ~50″ to the southeast, which shows prominent but compact Lyα emission (not shown in Fig. 6). The discarded candidates were either clearly extended continuum sources or line emitters associated with sources with photometric or spectroscopic redshifts incompatible with Lyα. We note that we use rather permissive search parameters in order to be able to spot even the fainter Lyα halos.

We also study the strength of the Lyα overdensity in relation with Hα. For this, we analyze the Lyα emission of the spectroscopic sample of Hα emitters in the MUSE datacube centered in A2744-45924, as well as in the data presented in Richard et al. (2021) centered in the A2744 cluster. We note that the depth of the observations from Richard et al. (2021) is comparable to that of our main dataset, with 3.5–7 h of on-source exposure, depending on the specific area; but, since we select all the sources from the homogeneous NIRCam images from their Hα emission, the differences between the MUSE datasets only have an impact on the accuracy of the individual Lyα measurements, thus not affecting our results. The FoV of both MUSE cubes are covered by NIRCam grism spectroscopy by the ALT survey that probes Hα at $3.8 < z < 5.1$. Matthee et al. (2025) found evidence for a large overdensity ($1 + \delta_{1\,\mathrm{cMpc}} \approx 30$) of galaxies (H$\alpha$ emitters) around A2744-45924. A discussion about the galaxy overdensities in the A2744 field is found in Naidu et al. (2024). Likewise, the detection of 4 prominent Lyα halos in the neighborhood of A2744-45924 indicates an excess of Lyα emission with respect to random. To determine whether excess ionizing radiation – such as that produced by the AGN in A2744-45924 – has enhanced the photoionizing background and contributed to the excess Lyα emission from halos around A2744-45924, we must account for the underlying galaxy overdensity. The excess of Lyα emission in $z = 4.464 \pm 0.02$ in the FoV of both MUSE fields is $\delta + 1 \approx 20$ (comparing with the mean value in our data), while the excess of Hα is $\delta + 1 \approx 54$, when comparing the total flux of these lines with respect to the mean across $z = 3.8$–5.5 in the same footprint.

We first extract MUSE spectra of all the Hα emitters in the ALT spectroscopic catalog using as extraction mask the morphology of the Hα emission, as described in Mascia et al. (in prep.). The Lyα profile is then fitted in the 1D spectrum with a double skewed Gaussian to obtain priors for the line parameters, specifically the red peak wavelength and FWHM. Then, we re-extract Lyα, this time accounting for possible extended halos. To achieve this, we construct optimal weight masks by collapsing the MUSE datacubes along the spectral direction within a range defined by the FWHM and peak position of the red Lyα component. We mask pixels below a S/N threshold of 3 after applying a Gaussian smoothing kernel with $\sigma = 2$ px. Finally, we re-extract the spectra of all Hα emitters and measure the Lyα fluxes by performing a fits to double skewed Gaussian profiles.

Figure 7 shows the ratio between the observed Lyα and Hα emission from the Hα emitters within the two deep MUSE cubes in the A2744 field. We highlight the average Lyα to Hα ratio at the redshift of A2744-45924. Our main finding is that despite the large overdensity of Hα emitters, the Lyα produced by these sources is moderate to low in comparison with other overdensities in the field, yet within the typical values (mean Lyα/Hα = 0.4, standard deviation 0.3). This result makes it unlikely that the observed Lyα halos near A2744-45924 could be partly powered by its AGN, via scattering of Lyα or photoionization (e.g., Cantalupo et al. 2014). Moreover, A2744-45924 has three very close neighbors (angular separation <3″, <15 pkpc in projection, $\Delta z \lesssim 0.02$; $\Delta v \lesssim 1000$ km s^{-1}), which totally lack detection of

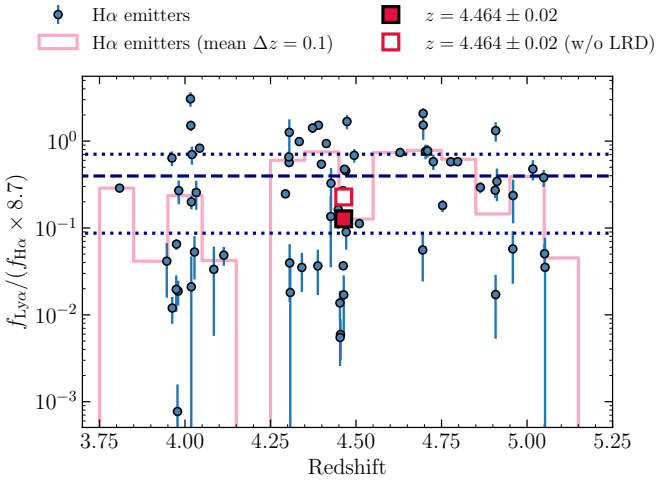

Fig. 7. Ratio of total Lyα to Hα flux for all the Hα emitters in the FoV of the MUSE data presented in this work, and the data from Richard et al. (2021) in the A2744 cluster. We include a 1/8.7 factor for direct comparison with the Case B ($T = 10^4$ K) ratio. The dashed and dotted blue lines show the mean and standard deviation in the field, respectively. We note that the fluxes are not dust-corrected. We show the total flux ratio variation in bins of redshift $\Delta z = 0.1$ (pink line), and within $\Delta z = 0.02$ around the redshift of A2744-45924, itself included (red filled square) and excluded (empty square). The Lyα/Hα ratio in the environment of A2744-45924 is moderate in comparison with other overdensities in our data, despite the large intrinsic overdensity of Hα emitters (Labbe et al. 2024; Matthee et al. 2025).

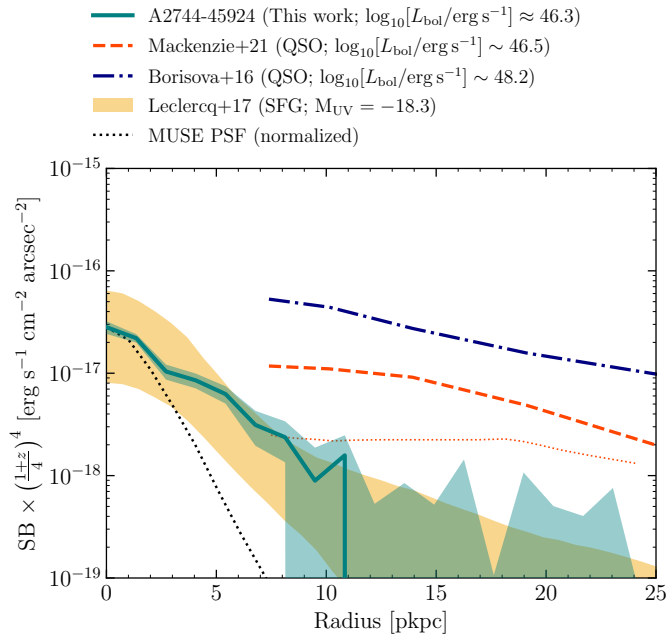

Fig. 8. Radially average surface brightness (SB) profile of the Lyα emission of A2744-45924. Shown are the SB profile measured in the MUSE image (teal solid line; the shaded area gives the 1σ dispersion), and the SB produced by a point source for reference (black dotted line), normalized to the peak Lyα emission of A2744-45924. We compare our measurements to the halos measured around star-forming galaxies ($3 < z < 6$; $-22 < M_{UV} < -15$; Leclercq et al. 2017, shaded orange region between 16th and 84th percentiles), and also to Lyα halos of quasars at $z \sim 3.2$ (blue dot-dashed and orange dashed lines, Borisova et al. 2016; Mackenzie et al. 2021, respectively). The Lyα halo of A2744-45924 is comparable to that of SFGs both in terms of absolute SB and exponential scale length, despite having L_{bol} comparable to that of quasars from Mackenzie et al. (2021). For reference, we also plot the faintest quasar halo in Mackenzie et al. (2021) as a dotted orange line.

Lyα emission despite being detected in Hα ($L_{H\alpha} \approx 10^{42}$ erg s^{-1}), hence, there is no evidence that any escaping ionizing radiation from A2744-45924 is significantly affecting the CGM of these galaxies.

5. What powers the Lyα emission from A2744-45924?

5.1. A weak halo for an extremely bright LRD

We begin by investigating the origin of the Lyα emission by analyzing the properties of the extended Lyα halo of A2744-45924. Extended Lyα nebulae are ubiquitous around bright quasars (Borisova et al. 2016; Arrigoni Battaia et al. 2019). Mackenzie et al. (2021) reported a 100% detection rate of Lyα halos around fainter quasars[4], with extensions exceeding 60 pkpc. They also found that the extent of quasar Lyα halos remains roughly independent of source luminosity, differing only by a normalization factor. In contrast, we find a relatively compact Lyα halo around A2744-45924, whose surface brightness profile[5] is shown in Fig. 8. Fitting an exponential profile to this halo yields a scale length of $h = 5.7 \pm 0.7$ pkpc (see Sect. C.1).

Figure 8 compares the Lyα surface brightness profile of A2744-45924 with that around star-forming galaxies from Leclercq et al. (2017), as well as halos powered by luminous quasars ($M_{UV} \approx -29$) from Borisova et al. (2016) and fainter quasars ($M_{UV} \approx -25$) from Mackenzie et al. (2021). The distinction between these populations is evident: quasar halos exhibit flatter profiles and extend over significantly larger distances.

As inferred from the Hα luminosity and FWHM, A2744-45924 shows a very high bolometric luminosity $\log_{10}(L_{bol}/erg\,s^{-1}) = 46.3 \pm 0.2$ (see Matthee et al. 2025, and references therein), placing it in the regime of luminous quasars (Shen et al. 2020). For comparison, the average bolometric luminosities in Borisova et al. (2016) and Mackenzie et al. (2021) are $\log_{10}(L_{bol}/erg\,s^{-1}) \approx 48.2$ and 46.5, respectively, estimated using the bolometric corrections from Richards et al. (2006). The latter is comparable to the Hα-inferred bolometric luminosity of A2744-45924, yet their Lyα halos are ~10 times brighter. However, the validity of standard scaling relations for LRDs is uncertain, so L_{bol} could be overestimated. Mackenzie et al. (2021) reported a tentative relation between L_{UV} and the Lyα halo luminosity. Extrapolating their results, we obtaing that L_{bol} would need to be overestimated by $\gtrsim 2$ dex for the 1σ limit to match the average SB in Mackenzie et al. (2021). In turn, the halo of A2744-45924 is consistent with the halos found by Leclercq et al. (2017) around star-forming galaxies with M_{UV} between −15 and −22 (A2744-45924 has $M_{UV} = -19.39^{+0.12}_{-0.10}$), which have a median scale length of $h = 4.5$ pkpc (ranging from 1 to 18 pkpc). Overall, we find no evidence that the AGN in A2744-45924 is leaking enough ionizing photons to power a Lyα halo like those observed around quasars with similar

[4] However, see also Herenz et al. (2015), who reported 0% detection rate in five radio-quiet quasars.

[5] The SB was measured in radii intervals in the source plane, considering radial and transverse magnification factors of $\mu_t = 1.68$, $\mu_r = 1.07$, and a shear angle $\theta_\mu = 19.9°$ (Furtak et al. 2025; Price et al. 2025).

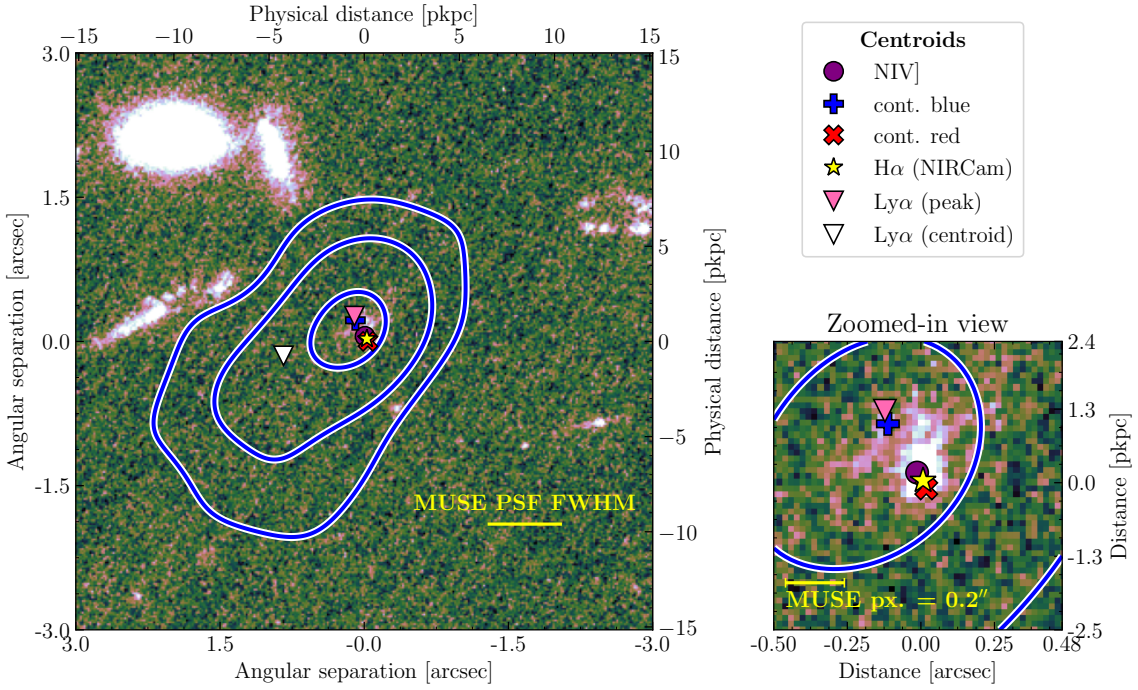

Fig. 9. Lyα contours and centroids of different spectral components of A2744-45924, over the NIRCam F070W cutout. Shown are contours corresponding to 10%, 50%, and 90% of the peak Lyα flux (see Sect. 3.3). Also shown are the flux averaged centroids of the point-like NIRCam Hα emission (yellow star), the MUSE collapsed continuum in the ranges 1235–1430 Å (*cont. blue*) and 1555–1712 Å (*cont. red*; blue and red crosses); the centroid of the NIV] (purple circle) and Lyα lines (white triangle); as well as the position of the peak Lyα (pink triangle). The bottom right panel shows a zoomed-in view of A2744-45924. The spatial centroid of *cont. red* is consistent with the centroids of the NIRCam and the position of NIV], while *cont. blue* is shifted toward the position of the peak Lyα and the diffuse extended component in F070.

bolometric luminosities, either in terms of scale length or absolute surface brightness.

5.2. Spatial shift of UV continuum and Lyα emission

Our data revealed different spatially resolved components of A2744-45924: extended Lyα emission (Sect. 3.3), two rest-frame UV continuum components (Sect. 3.2), and a spatially compact NIV] emission line (Sect. 3.5, Fig. 5). In Fig. 9 we show the contours of the Lyα halo, overimposed on the F070W image, and we mark the spatial positions of the centroids of the MUSE continuum components and NIV], peak Lyα, and the coordinates of Hα from NIRCam. Although the PSF of NIRCam and MUSE are very different, it is clear that the peak of the Lyα emission is consistent with the center of the diffuse extended component seen in F070W (see Fig. 1). Both these peaks are shifted ∼0.2″ from the core component that marks the position of the AGN.

The unresolved morphology of NIV] might suggest that it is originated close to the AGN component (see Sect. 3.5). We fit a 2D Gaussian with FWHM = 0.65″ (for comparison, MUSE average effective PSF of 0.75″), whose center is shown in Fig. 9. The centroid of the NIV] emission aligns with *cont. red* and the NIRCam centroids. In addition, we compute the UV colors for the components fitted to the NIRCam F070W and F090W images, fixing the morphology of both components (see Appendix A). Although the Lyα contamination in F070W and possible model degeneracies complicate the interpretation of these UV colors, we obtain F070W – F090W = 1.48 for the compact component, aligned with Hα (AGN-associated); and 0.45 for the slighly more extended component (host galaxy-associated), respectively. Consistent with our findings from MUSE, the AGN component appears redder and declines steeply from F090W to F070W, while the host galaxy component remains relatively blue. We note that the F070W band covers the rest-frame 1142–1429 Å, extending blueward Lyα, hence its flux is potentially affected by the Lyα forest absorption.

From the spatial offset between the Lyα peak and the core component (Fig. 9) it is suggested that no significant Lyα is emitted directly by the core along our line of sight. Additionally, the shift of the UV continuum centroid toward the Lyα peak at bluer wavelengths implies that the Lyα emission likely originates from this component. This is consistent with a scenario in which the core continuum is suppressed and a shifted component with bluer rest-UV colors dominates in the far-UV. The alignment of the compact NIV] emission with the JWST coordinates of Hα ensures that our measured Lyα to UV offset is robust against WCS uncertainties. The question to answer is whether the Lyα emission is powered by star formation in a host galaxy or by the AGN through resonant scattering or photoionization.

5.3. Can star formation power the Lyα emission?

In star-forming galaxies at $z \approx 0$–2, observations have shown that the observed EW of Lyα correlates with $f_{\rm esc}$(Lyα) (Verhamme et al. 2017; Sobral et al. 2017). A2744-45924 shows a fairly high Lyα EW$_0$ = 97 ± 28 Åwith a narrow line-profile (FWHM = 270 ± 15 km s^{-1}), suggesting a moderate $f_{\rm esc}$(Lyα) = 0.48 ± 0.18 (Sobral & Matthee 2019). If the Lyα emission of the halo is produced by star formation, we should see the corresponding component of Hα in the grism data, with a total flux of (2.4 ± 0.7) × 10^{-18} erg s^{-1} cm^{-2} (magnification corrected and

assuming a ratio of Lyα/Hα = 8.7). However, this component is likely outshined by the broad Hα emission from the central engine, with a flux of $\approx 40 \times 10^{-18}$ erg s^{-1} cm^{-2}, which we could not disentangle in the grism spectrum. Chen et al. (2025) identified the extended component of A2744-45924 as a star-forming galaxy with a blue rest-frame UV slope ($\beta_{\rm UV} = -2.12$) and little dust attenuation. We estimate the star formation rate needed to power the Lyα emission from A2744-45924 following Eq. (8) in Sobral & Matthee (2019), obtaining $\mathrm{SFR}_{\mathrm{Ly}\alpha} = 4.5 \pm 2.7\,\mathrm{M}_\odot\,\mathrm{yr}^{-1}$ (assuming $f_{\rm esc}$(LyC) = 0). We compare this value with the SFR obtained from the UV luminosity. From the morphological model of F090W (Sect. 3.1), we measure the UV luminosity subtracting the more compact component (assuming it is originated from the AGN), and obtain $M_{\rm UV} = -18.8 \pm 0.10$, whilst the value from the full morphological model is $M_{\rm UV} = -19.4 \pm 0.1$. For comparison, measuring the continuum from the MUSE optimally extracted spectrum, after masking emission lines, we likewise obtain $M_{\rm UV} = -19.39^{+0.12}_{-0.10}$. The star formation rate associated with the UV luminosity minus the compact component is $\mathrm{SFR}_{\rm UV} = 3.6 \pm 0.3\,\mathrm{M}_\odot\,\mathrm{yr}^{-1}$ (Kennicutt & Evans 2012), fully compatible with the SFR inferred from Lyα. This result suggests that the Lyα emission of A2744-45924 can be fully powered by star formation from the extended host galaxy, without any contribution from AGN photoionization or scattering.

6. Implications for the nature of A2744-45924

6.1. A fully enshrouded SMBH

Our results clearly indicate that Lyα emission in the A2744-45924 system is not centered on the main UV component (which almost certainly hosts an AGN, based on the co-spatial luminous and broad Hα emission), but rather on the secondary UV component, probably a star-forming companion or satellite of the former. Furthermore, as discussed in Sect. 5, the extended Lyα emission appears consistent in luminosity, size and EW with being powered by star formation in the secondary UV component, with little or no influence from the AGN, despite its high Hα-inferred bolometric luminosity and close proximity ($\sim$1.7 pkpc in projection, after correcting for magnification).

Here we discuss how these findings can be reconciled with the fact that Type 1 AGN with a similar intrinsic luminosity are invariably surrounded by significantly more luminous and extended Lyα nebulae (e.g., Mackenzie et al. 2021). One possibility is that the $L_{\rm bol}$ of A2744-45924 derived from $L_{\rm H\alpha}$ is overestimated by more than 2 dex (see Sect. 5.1), so that the true intrinsic bolometric luminosity of A2744-45924 is much lower, falling into a regime for which the ubiquity of luminous and extended Lyα nebulae has not been conclusively established yet. However, a simple explanation for the lack of a luminous Lyα nebula centered on it could be that the AGN photons usually responsible for powering Lyα emission do not reach the surrounding CGM due to some form of nuclear obscuration.

An obscuration scenario is qualitatively consistent with the fact that A2744-45924 (as well as other LRDs) is a Type 2 AGN, thence obscured at least along our line of sight. Obscuration only along our line of sight (with a covering factor $f_{\rm cov} \ll 1$), however, would not be sufficient to explain our findings, as AGN photons escaping in other directions would still be able to power a luminous Lyα nebula, as observed for instance around other Type 2 AGN (e.g., den Brok et al. 2020). Our findings therefore suggest that the obscuring material around the AGN in A2744-45924 (and possibly other LRDs) is likely to a have a large covering factor $f_{\rm cov} \sim 1$. This is consistent with the fact that the unobscured counterparts of LRDs has not yet been observed – That is, objects with similar broad Hα luminosities and similar number density, but bluer colors. A high $f_{\rm cov}$ scenario is also consistent with the hypothesis, recently brought forward to explain LRDs, of a SMBH covered by a very dense envelope of gas (Inayoshi & Maiolino 2025; Ji et al. 2025; Rusakov et al. 2025; Naidu et al. 2025; de Graaff et al. 2025), the so-called BH* model.

6.2. Fate of AGN ionizing and Lyα photons

To gain further insight on the implications of our observations for the properties of the obscuring gas, we need to make assumptions on the exact powering mechanism for AGN Lyα nebulae, thence the wavelength range of the photons that need to be obscured in the case of A2744-45924 and in turn the properties of the material that could be responsible for the obscuration. The dominant emission mechanism for AGN-powered Lyα nebulae is not fully clear and still subject to debate, the two most commonly invoked mechanisms being recombination and resonant scattering (e.g., Cantalupo et al. 2014)[6].

In the first scenario (recombination), ionizing photons reach and ionize the CGM, triggering the emission of recombination lines including Lyα. If this interpretation is correct (as indicated for instance by the detection of nonresonant recombination lines from at least some AGN-powered Lyα nebulae; e.g., Langen et al. 2023), then our main result—the *lack* of a luminous and extended Lyα nebula centered on the AGN – suggests a high covering factor of material that is optically thick to hydrogen-ionizing photons, requiring neutral hydrogen column density $N_{\rm H\,I} > 10^{17.2}\,\mathrm{cm}^{-2}$. This is very consistent with (albeit not conclusive proof of) the BH* model, which predicts $N_{\rm H\,I} \sim 10^{24}\,\mathrm{cm}^{-2}$, fully sufficient to completely suppress the hydrogen ionizing flux, but is also subject to caveats, as discussed in Sect. 6.3 below.

In the second scenario (scattering), part of the Lyα photons from the AGN broad line region (BLR) reach the CGM and are scattered by neutral hydrogen atoms therein into our line of sight. The Lyα to Hα ratio within $\sim$135 km s^{-1} around the Lyα centroid is $\sim$0.07, implying that a Lyα escape fraction of $\sim$10% (assuming case B recombination) would be sufficient, making this scenario energetically feasible ($f_{\rm esc}$(Lyα) < 1), although it may be difficult to reconcile with the high gas densities inferred from other diagnostics. Under the scattering hypothesis, the observed lack of a luminous Lyα nebula implies a high $f_{\rm cov}$ of obscuring material which is able to destroy AGN Lyα photons. Intriguingly, this is also in line with the observed lack of broad Lyα emission from A2744-45924. We note that this observation could in principle be explained by a proximate damped Lyα (PDLA) system (e.g., Marino et al. 2019). This interpretation, however, is disfavored by the fact that a similar lack of broad Lyα emission is also observed in other LRDs (e.g., Ning et al. 2024), suggesting, on statistical grounds, that the suppression of AGN Lyα photons is more likely due to an absorbing medium intrinsic to the system and surrounding the AGN with high $f_{\rm cov}$.

One possible agent for the destruction of Lyα photons is dust. However, dust obscuration is disfavored in A2744-45924 by the observed flat rest-IR slopes by NIRCam/MIRI and the far-IR and radio nondetections (Spitzer/Herschel, ALMA), which

[6] A third mechanism, collisional excitation, is also expected to play a role in extended Lyα emission around galaxies (e.g., Dijkstra & Loeb 2009) but is disfavored for AGN nebulae due to photo-ionization effects (e.g., Pezzulli & Cantalupo 2019).

indicate no significant emission of reprocessed light by hot dust (Setton et al. 2024). On the other hand, we recall that resonant scattering of Lyα photons through a large column density of neutral hydrogen – as expected in the envelope of a BH* – increases the effective path length of Lyα photons, and therefore the efficiency of dust-induced suppression also for relatively low dust content (Scarlata et al. 2009). For example, even for low values of dust attenuation such as $A_V \approx 0.1$, one can obtain, for a static medium with $N_{\rm H\,I} = 10^{20}\,{\rm cm^{-2}}$ ($10^{21}\,{\rm cm^{-2}}$), escape fractions as low as $f_{\rm esc,Ly\alpha} \sim 0.03$ (0.004) (Neufeld 1990; Calzetti et al. 2000; Verhamme et al. 2006). Overall, there is no evidence that Lyα photons from the AGN in A2744-45924 are being destroyed by dust, but this possibility cannot be fully discarded without more detailed modelling.

Another mechanism for Lyα suppression is efficient l-changing (2p→2s) collisions. A Lyα scattering event can be described as a succession of one Lyα absorption, inducing a transition of a neutral hydrogen atom from the 1s state to the 2p state, followed by spontaneous re-emission, accompanied by a decay back to the ground level (2p→1s). It is possible, however, that between these two events, a collision – for instance with a proton – induces an l-changing transition from the 2p state to the 2s state, from which Lyα emission is not permitted. The transition back to the ground level will then occur through either two-photon decay (for $n \lesssim 10^4\,{\rm cm^{-3}}$) or collisional de-excitation (for $n \gtrsim 10^4\,{\rm cm^{-3}}$; Spaans & Silk 2006; Neufeld 1990), in either case resulting in the effective destruction, rather than scattering, of the initial Lyα photon. For each scattering event, an l-changing (2p→2s) collision, resulting in the destruction of a Lyα photon, is the most likely outcome only for extremely high densities $n_p \gtrsim n_{\rm p,crit} = A_{\rm Ly\alpha}/q_{\rm 2p2s} = 3.5 \times 10^{12}\,{\rm cm^{-3}}$, where $A_{\rm Ly\alpha} = 6.25 \times 10^8\,{\rm s^{-1}}$ is the Einstein coefficient for Lyα emission and $q_{\rm 2p2s} = 1.8 \times 10^{-4}\,{\rm cm^3\,s^{-1}}$ is the coefficient for a proton-induced 2p→2s collisional transition (Dijkstra et al. 2016). However, even for densities $n_{\rm p} \ll n_{\rm p,crit}$, repeated scatterings across a path with high $N_{\rm H\,I}$ boosts the probability of a Lyα photon being destroyed before escaping the system. Along similar lines as in Dijkstra et al. (2016), the number of required scattering events for Lyα destruction can be estimated as $N_{\rm scatt} = n_{\rm p,crit}/n_{\rm p}$. For the fiducial density $n_{\rm e} \sim 10^9\,{\rm cm^{-3}}$ of the BH* model (Naidu et al. 2024), a number of scatterings $N_{\rm scatt} = 3.5 \times 10^3$ would be sufficient, achievable (for a static medium and at line center) with a neutral hydrogen column density $N_{\rm H\,I} \gtrsim 6{\times}10^{16}\,{\rm cm^{-2}}$ (see Equation (3) in Dijkstra et al. 2016) and abundantly met for $N_{\rm H\,I} \sim 10^{24}\,{\rm cm^{-2}}$, as in the BH* models. A more detailed analysis of this scenario would require taking into account the impact of kinematical effects, such as turbulence or possible inflow or outflow motions, on Lyα radiative transfer and is left for future investigation[7].

Overall, our findings provide support for the presence of obscuring material with a large covering factor ($f_{\rm cov} \sim 1$) of neutral hydrogen with at least a column density ($N_{\rm HI} \gtrsim 10^{17.2}\,{\rm cm^{-2}}$) around the AGN at the center of A2744-45924. Furthermore, under the assumption that the dominant emission mechanism for AGN-powered Lyα nebulae is Lyα scattering, our observations appear fully consistent with the high gas density and hydrogen column densities expected in the envelope of a BH*. We finally note that if LRDs have a higher than typical H$\alpha/L_{\rm bol}$ ratio (e.g., de Graaff et al. 2025), this could be in agreement with a scenario with $f_{\rm cov} \sim 1$, where a large fraction of ionizing photons would be expected to be reprocessed into recombination lines (including Hα) rather than escaping to large distances.

6.3. Origin of the compact UV emission and high-ionization emission lines

Another important aspect to address, in the context of nuclear obscuration with $f_{\rm cov} \sim 1$, is the nature of the main compact UV component in A2744-45924, as well as the presence of the emission lines of highly ionized species, such as O III], N IV], and C IV, in the spectrum (see Section 3.5 above, and Labbe et al. 2024). In one of the scenarios explored by Labbe et al. (2024), the UV portion of the spectrum of A2744-45924 could represent AGN light escaping through unobscured channels and being scattered by free electrons into our line of sight. This scenario would imply $f_{\rm cov} < 1$ and could also naturally explain the presence of high-ionization emission lines. Quantitatively, however, further work would be needed to determine the minimum fraction of the free (unobscured) solid angle ($f_{\rm uncov} = 1 - f_{\rm cov}$) required to explain the observed UV and line fluxes in this scenario and verify whether it is consistent with $f_{\rm uncov} \ll 1$, as indicated by our findings in this work.

A second scenario considered by Labbe et al. (2024) is that the UV spectrum may be dominated by a young, compact and metal-poor stellar population, which, in the context of the present discussion, could be interpreted as a compact nuclear star cluster surrounding the SMBH and its envelope. Because in this scenario the UV light originates outside the obscuring envelope, it would be consistent with $f_{\rm cov} = 1$, provided that the high-ionization emission lines were powered by star formation rather than the AGN. This would be somewhat unusual, considering the high ionizing potential for producing N IV] and C IV, but perhaps not impossible considering the very blue observed slope ($-\beta_{\rm UV} = 2.2$–2.9; Labbe et al. 2024), plausibly accompanied by an ionizing spectrum correspondingly harder than usual (Topping et al. 2025). This picture could also be supported by our finding that the N IV]λ1486 line is quite narrow (FWHM $\sim 270\,{\rm km\,s^{-1}}$; see Sect. 3.5), and therefore possibly arising from the interstellar medium (ISM) rather than the immediate proximity of the accretion disc. We note, in particular, that the relatively high density $n_{\rm H} \sim 10^5\,{\rm cm^{-3}}$ inferred from the f_{1483}/f_{1486} doublet ratio (Sect. 3.5) would in this case be indicative of a relatively dense ISM surrounding the even denser BH* envelope. For the implied ISM density $n \sim 10^5\,{\rm cm^{-3}}$, an ISM neutral hydrogen column density $N_{\rm H\,I} \sim 6 \times 10^{20}\,{\rm cm^{-2}}$ could already be sufficient to suppress also the Lyα photons from this hypothetical compact star-forming region through l-changing collisions, as well as any hydrogen-ionizing photons. This could possibly explain why such a nuclear star cluster is not in turn powering an extended Lyα halo centered on the compact source.

One third possibility is that the compact UV component is due to AGN photons that traverse the dense gas envelope without being entirely absorbed. The BH* scenario is designed so that a non-negligible fraction of the hydrogen atoms in the envelope is collisionally excited to the $n = 2$ level, capable of producing absorption features in Balmer lines, as well as producing a Balmer break by suppressing the Balmer continuum. Crucially, the photo-ionization cross-section for $n = 2 \rightarrow \infty$ (i.e., the Balmer continuum) transitions decreases with decreasing wavelength (roughly as $\propto \lambda^3$). Therefore, we can expect that for high but not extreme column densities, UV photons could be able to traverse the envelope, possibly explaining the emergence of a blue UV spectrum and consistent with $f_{\rm cov} = 1$. This scenario requires tailored modeling and will be the subject of future

[7] In the presence of differential motions with a constant velocity gradient, the required $N_{\rm H\,I}$ to obtain a given value of $N_{\rm scatt}$ is only increased by a factor $\sim v_{\rm max}/v_{\rm thermal}$ (Bonilha et al. 1979; Dijkstra et al. 2016).

investigation. We note that, if produced *within* the envelope (a few AU from the accretion disc in the model of Naidu et al. 2025), UV high-ionization emission lines, such as NIV] λ1486, would also, in principle, be able to traverse the envelope, with attenuated flux but conserved doublet ratio and EW. It would be more difficult, however, to explain the narrow width. If instead the NIV] λ1486 line is produced outside the envelope (as suggested by the small FWHM), this scenario would need either a nonvanishing $f_{\rm uncov}$ or some contribution from a compact young stellar population with a hard ionizing spectrum, as Lyman continuum photons encountering the envelope would be expected to be completely suppressed, in contrast to the Balmer continuum.

7. Summary

In this paper we presented MUSE observations of A2744-45924, an extremely bright LRD ($L_{H\alpha} \approx 10^{44}\,{\rm erg\,s^{-1}}$), revealing a narrow Ly$\alpha$ emission line, and a moderately extended Lyα halo. We summarize our main findings as follows:

1. A2744-45924 shows a narrow (FWHM $= 270 \pm 15\,{\rm km\,s^{-1}}$) single-peaked Ly$\alpha$ emission line, with ${\rm EW_0} = 97 \pm 28$ Åand a velocity separation of $\Delta v_{\rm red} = 183 \pm 5\,{\rm km\,s^{-1}}$ with respect to the systemic redshift. The Lyα emission has an extended spatial morphology, which can be well fitted by a combination of 2D Gaussian and exponential. The Lyα nebula has an exponential scale length of $h = 5.7 \pm 0.7$ pkpc and ellipticity $e = 0.46 \pm 0.05$ (Sect. 3.4).
2. We also report a significant (4σ) detection of NIV]λ1486, which exhibits a very compact spatial morphology. This emission line is associated with AGN activity, and the low ratio with the marginally detected (1.6σ) NIV]λ1483 suggest a high gas density (Sect. 3.5).
3. The Lyα emission peaks with a spatial offset of $\sim$0.2″ relative to the NIRCam centroid of the compact core of A2744-45924. This offset aligns with the position of the extended UV component seen in NIRCam. Additionally, the UV continuum detected with MUSE shows a shift toward shorter rest-frame wavelengths (1235–1430 Å) compared to longer wavelengths (1555–1712 Å). The spatial centroid of NIV] is consistent with the compact core, supporting its AGN origin and confirming that the observed Lyα and UV continuum shifts are not due to astrometry uncertainties (Sect. 5.2).
4. We investigated the Lyα emission of sources in the neighborhood of A2744-45924, in the MUSE field of $\sim 1.3' \times 1.3'$. We find four extended Lyα halos between 4.45 and 4.47 (in a volume corresponding to $\sim 172\,{\rm Mpc^3}$). We find an excess of total Lyα emission in an interval of $\Delta z = 0.02$ around A2744-45924 ($1 + \delta_{{\rm Ly}\alpha} \approx 20$). However, the ratio of the total Lyα to Hα flux is moderately low with respect to the average in the same FoV within $z = 3.75$–5.25, but still within 1σ. This result implies that A2744-45924 does not significantly enhance the Lyα luminosity of nearby halos through scattered Lyα light (Sect. 4).
5. The extended Lyα halo of A2744-45924 resembles those of star-forming Lyα emitters, more than quasars, in both scale length ($h = 5.7 \pm 0.7$ pkpc) and surface brightness (Leclercq et al. 2017). The narrow Lyα line contrasts with the broad Hα line (FWHM $\approx 4500\,{\rm km\,s^{-1}}$), suggesting different origins. We show that the Lyα emission can be fully explained by star formation in the host galaxy, without AGN contribution (Sects. 5.1 and 5.3).
6. We discuss the implications of our findings for a scenario in which the compact continuum emission and Hα are explained by a SMBH enshrouded in a dense cloud of gas (BH* models). We argue that the absence of a luminous Lyα halo, as seen in similarly bright Type I and II AGN, can be explained by obscuring neutral hydrogen gas with a covering factor $f_{\rm cov} \sim 1$ and column density $N_{\rm HI} \gtrsim 10^{17.2}\,{\rm cm^{-2}}$. However, the main caveat for these interpretations is that $L_{\rm bol}$ could be largely overestimated (Sects. 6.1 and 6.2).
7. Finally, we consider the implications of the UV continuum and high-ionization emission lines for the dense obscuring gas hypothesis. The observed properties are consistent with a BH* model with $f_{\rm cov} \sim 1$, although the exact interpretation depends on the gas distribution and geometry. Further modeling and observations are required to constrain the key parameters of the BH* model, i.e., $f_{\rm cov}$, $N_{\rm HI}$, $n_{\rm e}$ (Sect. 6.3).

Acknowledgements. We thank the anonymous referee for constructive and useful comments. We thank Sebastiano Cantalupo for comments on the draft. Based on observations collected at the European Organisation for Astronomical Research in the Southern Hemisphere under ESO programme 114.27M6.001. Funded by the European Union (ERC, AGENTS, 101076224). Views and opinions expressed are however those of the author(s) only and do not necessarily reflect those of the European Union or the European Research Council. Neither the European Union nor the granting authority can be held responsible for them. We acknowledge funding from JWST program GO-3516. This work is based in part on observations made with the NASA/ESA/CSA James Webb Space Telescope. The data were obtained from the Mikulski Archive for Space Telescopes at the Space Telescope Science Institute, which is operated by the Association of Universities for Research in Astronomy, Inc., under NASA contract NAS 5-03127 for JWST. These observations are associated with program #3516. MG thanks the Max Planck Society for support through the MPRG. FDE acknowledges support by the Science and Technology Facilities Council (STFC), by the ERC through Advanced Grant 695671 "QUENCH", and by the UKRI Frontier Research grant RISEandFALL. TU acknowledges funding from the ERC-AdG grant SPECMAP-CGM, GA 101020943. GK acknowledges support from the MERAC foundation.

References

Abell, G. O., Corwin, H. G., Jr, & Olowin, R. P. 1989, ApJS, 70, 1
Adamo, A., Atek, H., Bagley, M. B., et al. 2025, Nat. Astron., 9, 1134
Akins, H. B., Casey, C. M., Chisholm, J., et al. 2025a, ArXiv e-prints [arXiv:2503.00998]
Akins, H. B., Casey, C. M., Lambrides, E., et al. 2025b, ApJ, 991, 37
Ananna, T. T., Bogdán, Á., Kovács, O. E., Natarajan, P., & Hickox, R. C. 2024, ApJ, 969, L18
Arita, J., Kashikawa, N., Onoue, M., et al. 2025, MNRAS, 536, 3677
Arrigoni Battaia, F., Hennawi, J. F., Prochaska, J. X., et al. 2019, MNRAS, 482, 3162
Bacon, R., Accardo, M., Adjali, L., et al. 2010, SPIE Conf. Ser., 7735, 773508
Bacon, R., Conseil, S., Mary, D., et al. 2017, A&A, 608, A1
Bacon, R., Brinchmann, J., Conseil, S., et al. 2023, A&A, 670, A4
Barro, G., Perez-Gonzalez, P. G., Kocevski, D. D., et al. 2024, ArXiv e-prints [arXiv:2412.01887]
Bezanson, R., Labbe, I., Whitaker, K. E., et al. 2024, ApJ, 974, 92
Bonilha, J. R. M., Ferch, R., Salpeter, E. E., Slater, G., & Noerdlinger, P. D. 1979, ApJ, 233, 649
Borisova, E., Cantalupo, S., Lilly, S. J., et al. 2016, ApJ, 831, 39
Calzetti, D., Armus, L., Bohlin, R. C., et al. 2000, ApJ, 533, 682
Cantalupo, S., Arrigoni-Battaia, F., Prochaska, J. X., Hennawi, J. F., & Madau, P. 2014, Nature, 506, 63
Chen, C. H., Ho, L. C., Li, R., & Inayoshi, K. 2025, ArXiv e-prints [arXiv:2505.03183]
de Graaff, A., Rix, H.-W., Naidu, R. P., et al. 2025, A&A, 701, A168
den Brok, J. S., Cantalupo, S., Mackenzie, R., et al. 2020, MNRAS, 495, 1874
D'Eugenio, F., Maiolino, R., Perna, M., et al. 2025, ArXiv e-prints [arXiv:2503.11752]
Dijkstra, M., Gronke, M., & Sobral, D. 2016, ApJ, 823, 74
Dijkstra, M., & Loeb, A. 2009, MNRAS, 400, 1109
Erb, D. K., Steidel, C. C., & Chen, Y. 2018, ApJ, 862, L10
Erwin, P. 2015, ApJ, 799, 226
Furtak, L. J., Zitrin, A., Weaver, J. R., et al. 2023, MNRAS, 523, 4568
Furtak, L. J., Secunda, A. R., Greene, J. E., et al. 2025, A&A, 698, A227
Gloudemans, A. J., Duncan, K. J., Eilers, A.-C., et al. 2025, ApJ, 986, 130
Greene, J. E., Labbe, I., Goulding, A. D., et al. 2024, ApJ, 964, 39
Harikane, Y., Zhang, Y., Nakajima, K., et al. 2023, ApJ, 959, 39

Herenz, E. C., Wisotzki, L., Roth, M., & Anders, F. 2015, A&A, 576, A115
Horne, K. 1986, PASP, 98, 609
Inayoshi, K., & Maiolino, R. 2025, ApJ, 980, L27
Ji, X., Maiolino, R., Übler, H., et al. 2025, ArXiv e-prints [arXiv:2501.13082]
Juodžbalis, I., Ji, X., Maiolino, R., et al. 2024, MNRAS, 535, 853
Kennicutt, R. C., & Evans, N. J. 2012, ARA&A, 50, 531
Kewley, L. J., Nicholls, D. C., Sutherland, R., et al. 2019, ApJ, 880, 16
Kocevski, D. D., Onoue, M., Inayoshi, K., et al. 2023, ApJ, 954, L4
Kocevski, D. D., Finkelstein, S. L., Barro, G., et al. 2025, ApJ, 986, 126
Kokorev, V., Caputi, K. I., Greene, J. E., et al. 2024a, ApJ, 968, 38
Kokorev, V., Chisholm, J., Endsley, R., et al. 2024b, ApJ, 975, 178
Labbe, I., Greene, J. E., Matthee, J., et al. 2024, ArXiv e-prints [arXiv:2412.04557]
Labbe, I., Greene, J. E., Bezanson, R., et al. 2025, ApJ, 978, 92
Langen, V., Cantalupo, S., Steidel, C. C., et al. 2023, MNRAS, 519, 5099
Latif, M. A., Aftab, A., Whalen, D. J., & Mezcua, M. 2025, A&A, 694, L14
Leclercq, F., Bacon, R., Wisotzki, L., et al. 2017, A&A, 608, A8
Leung, G. C. K., Finkelstein, S. L., Pérez-González, P. G., et al. 2025, ApJ, 992, 26
Lin, X., Fan, X., Wang, F., et al. 2025, ArXiv e-prints [arXiv:2504.08039]
Lin, X., Wang, F., Fan, X., et al. 2024, ApJ, 974, 147
Ma, Y., Greene, J. E., Setton, D. J., et al. 2025, ApJ, 981, 191
Mackenzie, R., Pezzulli, G., Cantalupo, S., et al. 2021, MNRAS, 502, 494
Maiolino, R., Scholtz, J., Curtis-Lake, E., et al. 2024a, A&A, 691, A145
Maiolino, R., Scholtz, J., Witstok, J., et al. 2024b, Nature, 627, 59
Maiolino, R., Risaliti, G., Signorini, M., et al. 2025, MNRAS, 538, 1921
Marino, R. A., Cantalupo, S., Pezzulli, G., et al. 2019, ApJ, 880, 47
Marques-Chaves, R., Schaerer, D., Kuruvanthodi, A., et al. 2024, A&A, 681, A30
Matsuoka, Y., Onoue, M., Iwasawa, K., et al. 2023, ApJ, 949, L42
Matthee, J., Pezzulli, G., Mackenzie, R., et al. 2020, MNRAS, 498, 3043
Matthee, J., Naidu, R. P., Brammer, G., et al. 2024, ApJ, 963, 129
Matthee, J., Naidu, R. P., Kotiwale, G., et al. 2025, ApJ, 988, 246
Mazzolari, G., Gilli, R., Maiolino, R., et al. 2026, A&A, in press, https://doi.org/10.1051/0004-6361/202453317
Naidu, R. P., Matthee, J., Kramarenko, I., et al. 2024, ArXiv e-prints [arXiv:2410.01874]
Naidu, R. P., Matthee, J., Katz, H., et al. 2025, ArXiv e-prints [arXiv:2503.16596]
Neufeld, D. A. 1990, ApJ, 350, 216
Niida, M., Nagao, T., Ikeda, H., et al. 2020, ApJ, 904, 89
Ning, Y., Cai, Z., Lin, X., et al. 2024, ApJ, 963, L38
Oke, J. B., & Gunn, J. E. 1983, ApJ, 266, 713
Pacucci, F., & Loeb, A. 2024, ApJ, 964, 154
Pérez-González, P. G., Barro, G., Rieke, G. H., et al. 2024, ApJ, 968, 4
Pérez-Montero, E., Contini, T., Lamareille, F., et al. 2013, A&A, 549, A25
Perger, K., Fogasy, J., Frey, S., & Gabányi, K. É. 2025, A&A, 693, L2
Pezzulli, G., & Cantalupo, S. 2019, MNRAS, 486, 1489
Pizzati, E., Hennawi, J. F., Schaye, J., et al. 2025, MNRAS, 539, 2910
Planck Collaboration VI 2020, A&A, 641, A6
Price, S. H., Bezanson, R., Labbe, I., et al. 2025, ApJ, 982, 51
Richard, J., Claeyssens, A., Lagattuta, D., et al. 2021, A&A, 646, A83
Richards, G. T., Lacy, M., Storrie-Lombardi, L. J., et al. 2006, ApJS, 166, 470
Rusakov, V., Watson, D., Nikopoulos, G. P., et al. 2025, ArXiv e-prints [arXiv:2503.16595]
Scarlata, C., Colbert, J., Teplitz, H. I., et al. 2009, ApJ, 704, L98
Setton, D. J., Greene, J. E., de Graaff, A., et al. 2024, ArXiv e-prints [arXiv:2411.03424]
Setton, D. J., Greene, J. E., Spilker, J. S., et al. 2025, ApJ, 991, L10
Shen, X., Hopkins, P. F., Faucher-Giguère, C.-A., et al. 2020, MNRAS, 495, 3252
Shibuya, T., Ouchi, M., Nakajima, K., et al. 2014, ApJ, 788, 74
Sobral, D., & Matthee, J. 2019, A&A, 623, A157
Sobral, D., Matthee, J., Best, P., et al. 2017, MNRAS, 466, 1242
Soto, K. T., Lilly, S. J., Bacon, R., Richard, J., & Conseil, S. 2016, MNRAS, 458, 3210
Spaans, M., & Silk, J. 2006, ApJ, 652, 902
Steidel, C. C., Bogosavljević, M., Shapley, A. E., et al. 2011, ApJ, 736, 160
Suess, K. A., Weaver, J. R., Price, S. H., et al. 2024, ApJ, 976, 101
Taylor, A. J., Finkelstein, S. L., Kocevski, D. D., et al. 2025a, ApJ, 986, 165
Taylor, A. J., Kokorev, V., Kocevski, D. D., et al. 2025b, ApJ, 989, L7
Topping, M. W., Stark, D. P., Senchyna, P., et al. 2025, ApJ, 980, 225
Tornotti, D., Fumagalli, M., Fossati, M., et al. 2025, ApJ, 980, L43
Treiber, H., Greene, J. E., Weaver, J. R., et al. 2025, ApJ, 984, 93
Urrutia, T., Wisotzki, L., Kerutt, J., et al. 2019, A&A, 624, A141
Vanden Berk, D. E., Richards, G. T., Bauer, A., et al. 2001, AJ, 122, 549
Verhamme, A., Orlitová, I., Schaerer, D., et al. 2017, A&A, 597, A13
Verhamme, A., Schaerer, D., & Maselli, A. 2006, A&A, 460, 397
Volonteri, M., Trebitsch, M., Greene, J. E., et al. 2025, A&A, 695, A33
Wang, B., Leja, J., de Graaff, A., et al. 2024, ApJ, 969, L13
Weibel, A., Oesch, P. A., Barrufet, L., et al. 2024, MNRAS, 533, 1808
Weilbacher, P. M., Palsa, R., Streicher, O., et al. 2020, A&A, 641, A28
Williams, C. C., Alberts, S., Ji, Z., et al. 2024, ApJ, 968, 34
Yue, M., Eilers, A.-C., Ananna, T. T., et al. 2024, ApJ, 974, L26

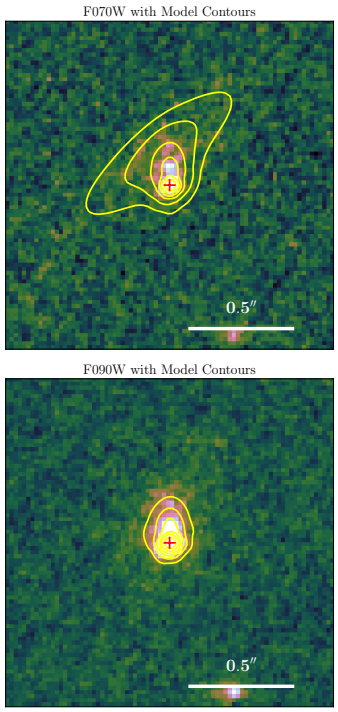

Fig. A.1. Same as in Fig. 1, but shown as contours for visual clarity. We draw contours at every factor 2 surface brightness decrease from the peak emission. A red cross marks the centroid of the Hα emission seen in NIRCam.

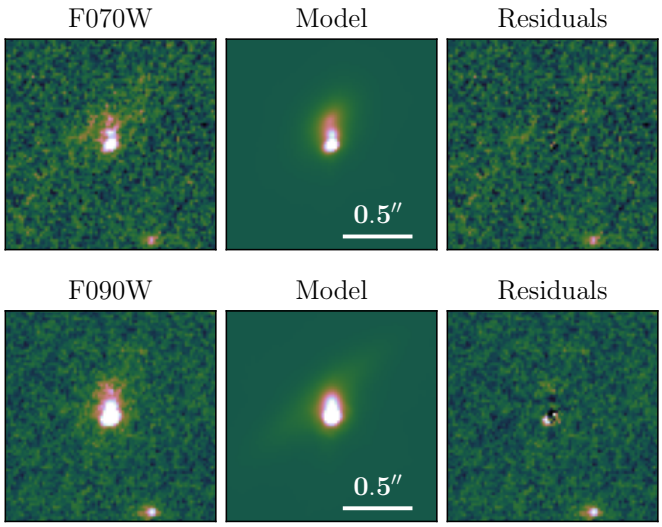

Fig. A.2. Alternative best-fit models of the UV morphology of A2744-45924 in the NIRCam filters F070W (top) and F090W (bottom). This figure is analogous to Fig. 1, but for each filter we apply the best-fitting model from the other filter, keeping its geometrical parameters fixed and allowing only the intensities to vary. The residuals of the extended component reveal that its geometry differs between the two filters. The more extended morphology seen in F070W may reflect a significant contribution from Lyα emission to the flux in this band.

Appendix A: Morphology fits to NIRCam F070W and F090W

In Sect. 3.1, we model the UV morphology of A2744-45924 in both F070W and F090W using two 2D elliptical Gaussians and one exponential component. The main difference between the fits in the two filters lies in the scale length of the exponential, which is significantly larger in F070W. In Fig. A.2, we present an alternative fitting approach in which the best-fitting model from F070W is used to fit the F090W image, and vice versa. In both cases, the positions and geometric parameters of all components are fixed to the best-fit values in one filter, allowing only the amplitudes to vary. The resulting residuals suggest that the geometry of the extended component is not consistent between filters, with F070W favoring a more extended exponential profile. This difference may point to a significant contribution from Lyα emission to the F070W flux.

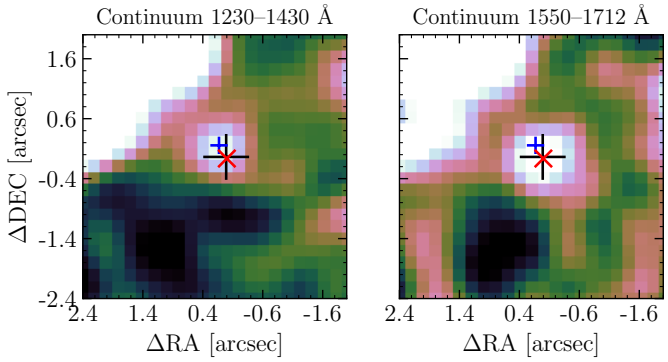

Fig. B.1. MUSE images of the continuum bands probing 1230–1430 Å (*cont. blue*) and 1550–1712 Å (*cont. red*). The centroid of the emission shows a clear shift of ≈0.2″. The centroids of these two components are shown in Fig. 9 in comparison with the positions of other spatially resolved spectral features. The bright source in the northeast corner is the blend of two low-z interlopers, clearly visible in Fig. 6. The black cross marks the NIRCam coordinates of A2744-45924. The blue and red crosses indicate the flux-weighted centroids of the blue and red continuum components, respectively.

Appendix B: Continuum centroids

In Fig. B.1 we show MUSE images, result of collapsing the datacube in the specified wavelengths. We deliberately avoid the rest-frame wavelength range in which N IV] and C IV are located, to capture only continuum emission. We observe a clear shift in the spatial centroid of the continuum, as can be visually seen in the Fig. B.1, with the black cross marking the NIRCam coordinates of A2744-45924 as reference. The flux weighted centroids of these components are shown in Fig. 9 ir relation to the positions of other spectral features (N IV], Lyα and NIRCam rest-frame UV centroids).

Appendix C: Lyα morphology fit

In Fig. C.1, we present the contours of the fitted model for the Lyα halo of A2744-45924. The fit was performed using the Python package LMFIT with the `leastsq` method. We tested various combinations of exponential and Gaussian components and found that a model consisting of one exponential and one Gaussian provided the lowest χ^2. We initially tested models including the morphology of NIRCam F090W (Sect. 3.1) as a core component at the position of A2744-45924 with a small shift to allow for astrometric uncertainties (see e.g., Matthee et al. 2020). However, we found that the fitting method could not satisfactorily constrain this component.

In Fig. C.2 we show the ellipses defined by the exponential fit to the Lyα halo at the exponential scale length. The image is

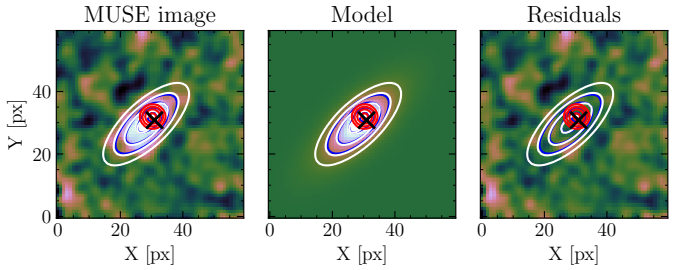

Fig. C.1. Morphological fit to the Lyα emission of A2744-45924. We fit a combination of the exponential (white), Gaussian (red), and a combination of the two (blue). The contours correspond to 80%, 40%, 20%, and 10% of the peak flux of each component. The JWST coordinates of A2744-45924 are marked with a black cross.

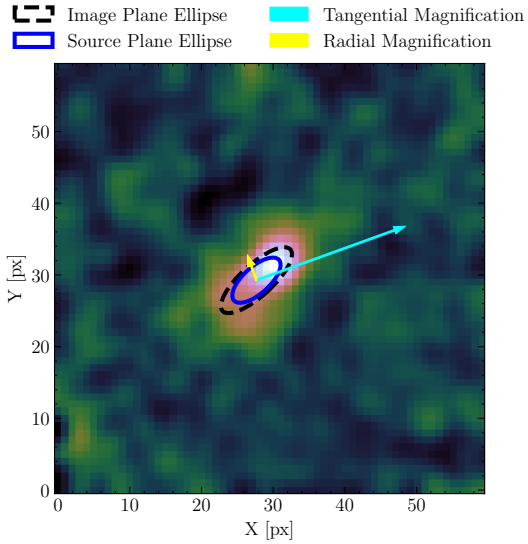

Fig. C.2. Ellipse defined by the fitted exponential at the scale length h in the image plane (dashed black) and the transformation into the image plane (dark blue). These ellipses are plotted over the MUSE image of the Lyα halo of A2744-45924 after applying a smoothing Gaussian filter of $\sigma = 1$ px. Also show are the directions of the radial and transverse magnification μ_r and μ_t (yellow and cyan arrows, respectively). The length of the arrows is proportional to $\mu_r - 1$ and $\mu_t - 1$ ($\mu_t = 1.68$, $\mu_r = 1.07$). the magnification in each direction.

more strongly magnified in the direction of the semi-major axis of the image. However, after applying the transformation to the source plane, the fitted exponential remains fairly elliptical with $e = 0.56$.

Appendix D: Spatial variations of the Lyα profile in the halo

We study the spatially resolved Lyα line profile of A2744-45924. For this, we fitted a skewed Gaussian defined as

$$f(v) = A \exp\left(-\frac{(v - v_0)^2}{2[a_{\rm asym}(v - v_0) + d]^2}\right) \quad \text{(D.1)}$$

(e.g., Shibuya et al. 2014) to every pixel in a box of $3'' \times 3''$ around the coordinates of A2744-45924, and after applying a Gaussian smoothing kernel with $\sigma = 2$ px in the spatial directions. In Fig. D.1 we show the spatial maps of three parameters of the skewed Gaussian: the peak velocity offset with respect to the systemic redshift $z = 4.464$ (v_0), the FWHM of the line profile,[8] and the asymmetry parameter ($a_{\rm asym}$).

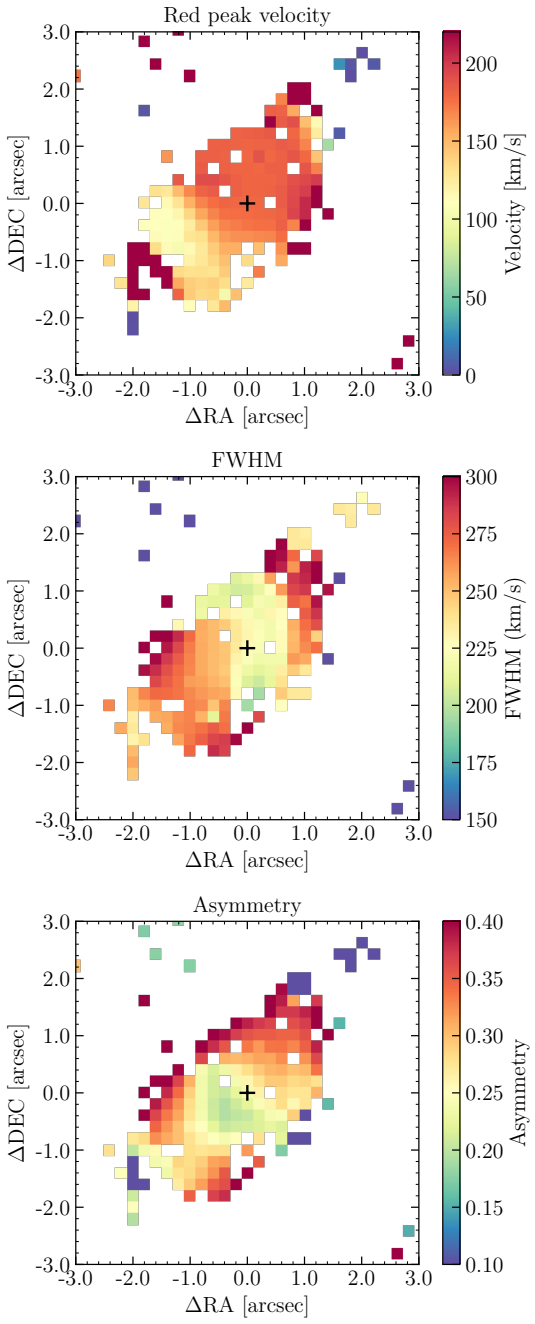

Fig. D.1. Spatial distribution of the fitted skewed Gaussian properties to the Lyα halo of A2744-45924. Shown are the velocity of the peak emission (top), the FWHM of the line in velocity space (middle), and the asymmetry parameter (see Eq. D.1; bottom). In these maps, we have masked out the pixels with a model amplitude (A in Eq. D.1) with S/N < 3. There are spatial variations of these parameters across the halo, in particular in a region with a slightly broader line profile and lower peak velocity toward the southwest. However, these differences are typical in Lyα halos of star-forming galaxies in the literature (e.g., Erb et al. 2018), and can be attributed to gas dynamics in the CGM.

[8] With the definition of skewed Gaussian of Eq. D.1, the full width at half maximum is obtained as FWHM = $\frac{2d\sqrt{2\ln 2}}{1-(2\ln 2)a_{\rm asym}^2}$